

Potential Vorticity Dynamics of Coastal Outflows

O. R. SOUTHWICK, E. R. JOHNSON, AND N. R. McDONALD

Department of Mathematics, University College London, London, United Kingdom

(Manuscript received 23 March 2016, in final form 21 February 2017)

ABSTRACT


A simple quasigeostrophic model is used to examine the outflow from a river, estuary, or strait into a coastal ocean. As shown by Johnson et al., these quasigeostrophic outflows are accurately described by analytical long-wave solutions. This paper first uses these solutions and contour dynamics simulations to discuss the behavior of coastal outflows. Second, it extends the model and the long-wave theory to consider the effects of ambient currents, tides, winds, or a variable source flux. Third, consideration of the momentum flux at the source is used to understand the turning of the current, showing that steady solutions conserve momentum, hence resolving the momentum imbalance paradox of Pichevin and Nof. Finally, a new numerical scheme to compute steady outflow boundaries is developed. The model focuses on the key dynamics driven by the source velocity and the generation of vorticity as the buoyant fluid adjusts. The simplicity of the model, and insight given by the long-wave solutions, enables a full understanding of the dynamics. The outflows display a range of behaviors, including indefinitely growing near-source bulges, steady boundary profiles with varying offshore width, bidirectional currents, and rarefying or eddy-like leading heads, all of which can be understood with the long-wave theory. Despite the simplicity of the model, the results show good agreement in comparison with observations, experiments, and numerical models.

1. Introduction

Outflows of buoyant fluid to the coastal ocean from rivers or straits connecting seas and ocean basins can be important features both dynamically and ecologically. More than a third of land-based rainfall travels to the ocean through rivers (Trenberth et al. 2007). The fluid in the source may have significantly different temperature, salinity, or depth to the ambient and will then adjust and gain relative vorticity as it is expelled (Spall and Price 1998). These differing properties may cause dramatic ecological effects, supporting marine ecosystems but also serving as sources of pollutants such as in the eutrophied dead zone of the Mississippi plume (Rabalais et al. 2002).

The dynamics of coastal outflows can be highly complex due to nonlinearity, the range of temporal and spatial scales, time dependence, and the significant number of influencing effects including buoyancy,

rotation, bathymetry, currents, tides, winds, and mixing. However, the dynamics can be understood and classified according to the Kelvin and Rossby numbers. Garvine (1995) identifies the Kelvin number, the ratio of the offshore length scale to the Rossby radius, as a key diagnostic of outflow dynamics. Small-scale outflows such as the River Teign in Devon or those close to the equator such as the Amazon have small a Kelvin number, so they are not affected significantly by rotation and tend to form radially spreading outflows. Outflows with a large Kelvin number, comprising large-scale, mid- and high-latitude outflows such as the Delaware and Rhine plumes and the Algerian and Norwegian coastal currents, are affected significantly by rotation. These typically form asymmetric outflows, which turn in the direction of Kelvin wave propagation, hereinafter referred to as “downstream” (rightward in the Northern Hemisphere, leftward in the Southern Hemisphere), and form coherent coastal currents stretching up to hundreds of kilometers along the coast.

 Denotes content that is immediately available upon publication as open access.

Corresponding author e-mail: Robb McDonald, n.r.mcdonald@ucl.ac.uk



This article is licensed under a [Creative Commons Attribution 4.0 license](http://creativecommons.org/licenses/by/4.0/) (<http://creativecommons.org/licenses/by/4.0/>).

The second key parameter is the Rossby number of the outflow. For narrow sources with high discharge, such as the Columbia River (Hickey et al. 1998; Horner-Devine 2009) and Hudson River (Chant et al. 2008) plumes, the Rossby number is sufficiently large that inertia is dynamically significant in the source region. In these cases a large, roughly circular bulge grows near the source and a much smaller coastal current carrying only a fraction of the source flux is formed (Avicola and Huq 2003; Horner-Devine et al. 2008). The bulge region is in gradient-wind balance but the coastal current is in geostrophic balance (Horner-Devine et al. 2006; Yankovsky and Chapman 1997). For wider sources, or when the outflow velocity is not as large, such as the Chesapeake Bay or Delaware Bay outflows, the Rossby number is low and the near-source region is in geostrophic balance, with a smaller bulge and more of the source flux entering the coastal current (Horner-Devine et al. 2015; Fong and Geyer 2002). Buoyancy is important in the dynamics of outflows, with the expelled fluid adjusting in depth and gaining vorticity via the stretching or squashing of vortex columns. While this generation of relative vorticity, or differences in potential vorticity from the source to the ambient fluid, is not always discussed explicitly in studies of outflows, it has been investigated in a number of works, including observational (Lake et al. 2005), experimental (Lane-Serff and Baines 2000), and modeling (Marques et al. 2014) studies of outflows, both through straits (Spall and Price 1998) and from rivers (Beardsley et al. 1985).

Outflows may also be surface advected or bottom trapped, with the Hudson Bay, Connecticut River, Chesapeake Bay outflow, and Mississippi River plumes being examples of surface outflows and the Rhine and Long Island Sound being bottom-trapped outflows (Horner-Devine et al. 2015). A number of factors such as variable outflow strength, ambient currents, tides, wind forcing, and a range of processes responsible for mixing may have significant effects on the dynamics of an outflow. The extent of the source of a coastal current can be anything from highly focused river outflows to extremely broad, almost continuous sources, such as along the Greenland coast (Chapman and Beardsley 1989). In this work, low Rossby number outflows are considered over the full range of Kelvin numbers and source width and velocity profiles, with the effects of variable source strength, ambient currents, tides, and winds also analyzed. In particular, observations of the Chesapeake Bay outflow will be used as a typical example to test and compare to a number of the results here.

The dynamical complexity of coastal outflows has led to theoretical investigations typically focusing on one particular aspect or area of the flow in isolation and

developing scalings or qualitative representations of the dynamics. A number of works have considered steady coastal currents with constant width. For example, the two-dimensional alongshore velocity and depth profiles of a rotating gravity current in a channel have been derived (Hacker and Linden 2002; Martin and Lane-Serff 2005; Martin et al. 2005). In experiments, the scalings of steady, geostrophic, constant-width coastal currents typically match well to the results (Davies et al. 1993; Lentz and Helfrich 2002; Avicola and Huq 2002; Thomas and Linden 2007).

The temporal development of vortical flows near boundaries and the effects of precursor Kelvin waves are discussed in Hermann et al. (1989). Kubokawa (1991) considered the formation of steady, constant-width currents from an outflow with a flux of zero potential vorticity fluid from the left-hand side of the source and a flux of negative potential vorticity fluid from the right-hand side of the source in a quasigeostrophic (QG) 1.5-layer model representing the outflow from the Tsugaru Strait, similar to the present approach. He showed that steady solutions do not always exist, in which case a bulge of outflow fluid confined near the source must grow. McCreary et al. (1997) performed simulations in a fully nonlinear 1.5-layer model with entrainment and horizontally varying salinity, for both low and moderate Rossby numbers. For low Rossby number, the results of this more complex model supported those of the simpler Kubokawa model.

It is important to understand where and when these steady, constant-width currents will form and how they attach to unsteady or variable-width parts of the flow by considering the full dynamics of the outflow. Johnson and McDonald (2006) considered an outflow of vortical fluid in the rigid-interface limit of the current problem (i.e., for zero Kelvin number) and derived an analytical expression for the steady boundary profile and velocity field, showing how the downstream constant-width current joined to a variable-width steady current near the source and an unsteady head downstream.

Other theoretical approaches have included conceptual models for the influence of winds on a river plume (Fong and Geyer 2001; Lentz 2004) or, for inertial outflows, modeling the bulge as a circular eddy with bottom “clipped” by the coast (Nof 1988). This clipped circle method appears to closely resemble bulges observed in laboratory (Avicola and Huq 2003) and numerical (Chen 2014) experiments for moderate Rossby number and has been used to diagnose the fraction of downstream transport in these experiments as a function of the “impact angle” of the outer bulge current, represented as a baroclinic jet, based on the theory of Whitehead (1985).

Another approach is to integrate the momentum equations over a control volume to deduce properties of the flow (Nof 1988; Pichevin and Nof 1997; Nof and Pichevin 2001; Nof et al. 2002; Nof 2005). Applying this technique, Pichevin and Nof (1997) deduced that steady, rightward-turning currents cannot conserve momentum and so are impossible—the so-called momentum imbalance paradox. To resolve this paradox, they suggest that the flow must be unsteady and either periodically produce westward-propagating eddies for a northward-oriented outflow on a β plane or have an indefinitely growing bulge near the source for non-northward outflows or those on an f plane. The significant implication of these results is that buoyancy and the Coriolis force are not sufficient to explain observations of steady rightward currents in the oceans and in experiments as previously thought. Instead, some other effect, such as an angled outflow, alongshore currents, or winds, must provide the momentum flux to turn the current in each one of these cases.

The approach of this paper is to develop and apply a model of outflows that captures the key dynamics yet is simple enough to easily interpret and to enable full mathematical analysis. The objective is that a complete understanding of this simple model can be used as a base to expand on and discuss the results of more sophisticated studies. The dynamics are analyzed in full before further effects and complexity are introduced. It will be seen that this model represents many aspects of outflows well. Considering the full spatial and temporal dynamics of the whole outflow shows when and where certain features will form. For example, there are situations in which steady solutions exist but are never realized by a flow evolving from a steady source.

The outflow is considered in a QG 1.5-layer model that captures the key dynamics: the rotation-modified source velocity and the generation of vorticity as the buoyant outflow adjusts. Although this model makes many simplifications, it is able to explore effects such as variable source outflow, ambient currents, tides, and winds. The strength of the model is its simplicity. This enables analytical solutions to be found for the boundary profile of the outflow and velocity field over time in many cases. These analytical solutions are derived for the primary problem of a constant strength outflow in Johnson et al. (2016, hereinafter JSM). Here, this theory is discussed in an oceanographic context and extended to consider the effects of a variable-strength source or ambient currents. The analytical solutions, along with numerical simulations, are used to build a detailed understanding of the dynamics of QG outflows.

Section 2 introduces the model and the analytical solutions given by JSM. Section 3 examines the primary

problem of a constant-strength outflow without ambient currents, tides, or winds. Sections 3a–c give results for the evolution of QG outflows comparing simulations and theory for zero, positive, and negative potential vorticity. Section 3d uses the momentum flux at the source to analyze the turning of the current and shows analytically and numerically that steady solutions conserve momentum. Appendix D presents a numerical scheme for computing steady boundary profiles for general outflows and gives an asymptotic steady boundary profile for the limit $a \rightarrow 0$. Section 4 extends the model to consider the effects of variable-strength sources, alongshore currents, tides, or winds. Conclusions and discussion are presented in section 5.

2. Quasigeostrophic model of a coastal outflow

The coast is modeled as a straight wall along the x axis and the river mouth as a source discharging fluid into an initially quiescent ocean occupying the upper half plane $y > 0$ (see Fig. 1). The source water is relatively lighter than the ambient, so it adjusts quickly and ageostrophically to a constant depth D . Let the source lie between $x = -L$ and $x = L$ and have depth D_s and volume flux $Q_0 D$, giving an area flux, once adjusted, of Q_0 , hereinafter simply referred to as the flux. To conserve potential vorticity (PV) as the expelled fluid adjusts, the squashing of vortex columns generates relative vorticity Π , which is constant, and positive if $D_s < D$ (Fig. 1b) or negative if $D_s > D$ (Fig. 1c). The unperturbed depth of the outflow D is constant so the PV Π/D is proportional to the generated relative vorticity Π and is constant, but takes the sign of Π so it may be positive or negative. Here, the focus is on the dynamics following this rapid ageostrophic adjustment period so the distance over which the outflow adjusts is taken to be negligible, compared to the other scales in the problem.

Coastal outflows are typically large scale but have shallow features. This work considers outflows without significant inertia (i.e., small Rossby number) over long periods, so an appropriate model is that of 1.5-layer QG flow. Let h be the small interface perturbation, f be the Coriolis parameter, g' be the reduced gravity, and $g' = g(\rho_2 - \rho_1)/\rho_2$ for gravitational acceleration g and upper and lower layer densities ρ_1 and ρ_2 . These give $\eta = g'h/f$, a streamfunction for the horizontal velocity $\mathbf{u} = (u, v)$, that is,

$$\mathbf{u} = \left(-\frac{\partial \eta}{\partial y}, \frac{\partial \eta}{\partial x} \right). \quad (1)$$

The QG PV is $(\nabla^2 \eta - \eta/L_R^2)/D$, for the Rossby radius of deformation $L_R = \sqrt{g'D}/f$, and is conserved so

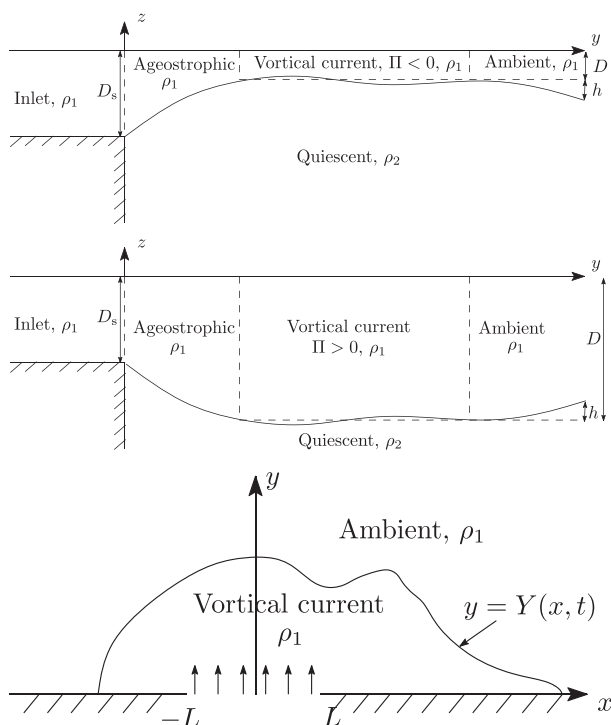


FIG. 1. The flow geometry near the inlet. (a) A side elevation of a vertical cut through the inlet region. Before the inlet is switched on, the ambient fluid in $y > 0$ is a two-layer quiescent fluid with density $\rho_1 < \rho_2$. Here the depth D_s of the inlet source is greater than the depth D of the upper-layer ambient fluid, and so the expelled fluid squashes vertically in a thin ageostrophic region matching to the exterior flow. The expelled fluid, occupying a region D , thus acquires negative potential vorticity Π . The disturbance to the interface height is given by $\eta(x, y, t)$. (b) As in (a), but for $D_s < D$, so the expelled fluid stretches vertically and acquires positive potential vorticity so $\Pi > 0$. (c) A plan view in the horizontal (x, y) plane showing the boundary $y = Y(x, t)$ of the vortical expelled fluid at some time $t > 0$.

$$\frac{D}{Dt} \left(\nabla^2 \eta - \frac{1}{L_R^2} \eta \right) = 0, \quad (2)$$

where D/Dt is the material derivative.

An arbitrary source velocity profile is imposed with the boundary condition on the coast $\eta(x, 0) = Q(x)$, where the source function $Q(x)$ ($\text{m}^2 \text{s}^{-1}$) is such that $Q(x) = 0$ for $x < -L$ and $Q(x) = Q_0$ for $x > L$. This can be thought of as a dam-break scenario where basins with surface heights $h = 0$ and $h = fQ_0/g'$ are separated by a wall with a gap. When the dam is released, the propagation of Kelvin waves rapidly establish the value $\eta(x, 0) = Q_0$ for $x > L$ along the right-hand coastline, with this process being instantaneous in the QG limit. The form of $Q(x)$ is related to the normal outflow velocity by

$$v(x, 0) = \frac{\partial Q}{\partial x}. \quad (3)$$

If \mathcal{D} is the domain occupied by the ejected fluid, bounded by $\partial\mathcal{D}$, then from (2)

$$\nabla^2 \eta - \frac{1}{L_R^2} \eta = \begin{cases} \Pi, & \text{inside } \mathcal{D}, \\ 0, & \text{outside } \mathcal{D}. \end{cases} \quad (4)$$

This equation, combined with the boundary condition specifying the source flux

$$\eta = Q(x), \quad \text{for } y = 0, \quad (5)$$

and the requirement that the fluid is quiescent far from the source

$$\nabla \eta \rightarrow 0, \quad \text{as } x^2 + y^2 \rightarrow \infty, \quad (6)$$

gives the streamfunction η . The fluid velocity can then be found using (1). The problem is closed with the initial condition that the source is switched on at $t = 0$ and the condition that $\partial\mathcal{D}$ is a material boundary, which, for outflows where $\partial\mathcal{D}$ can be expressed as $y = Y(x, t)$, can be written $D(y - Y)/Dt = 0$ on $y = Y(x, t)$ and rearranged to

$$Y_t = \{ \eta[x, Y(x, t)] \}_x, \quad (7)$$

where subscripts denote partial derivatives.

Equations (4)–(7) describe the evolution of the expelled vortical fluid. The velocity is determined by the streamfunction η , which is in turn completely determined by the shape of the curve $\partial\mathcal{D}$. Since the PV is piecewise constant, the evolution of this curve can be accurately and efficiently computed using the method of contour dynamics with surgery (Dritschel 1988).

If lengths in this problem are scaled on $\sqrt{Q_0/|\Pi|}$, the downstream width of a vorticity-driven current in the absence of background rotation (Johnson and McDonald 2006), and time on the vortical timescale $1/|\Pi|$, then the flow behavior depends on the sign of Π and on the ratio of the Rossby radius to the vortical length scale,

$$a = L_R \sqrt{\frac{|\Pi|}{Q_0}}. \quad (8)$$

JSM describe how the parameter a measures the ratio of the strengths of vortical effects to Kelvin wave-induced source flow and also show that the other nondimensional parameter L_R/L , for source width L , has little influence on the leading-order dynamics. For large a the dynamics are dominated by the anomalous vorticity, and for small a they are dominated by the source flow.

As section 3d notes, both the rotation-modified component of the source velocity and the vorticity contribute

fluxes of x momentum that can be used to understand the turning of the current. The relative importance of these two momentum fluxes is determined by a . When the outflow adjusts to a shallower level, Π is negative and the vorticity contributes negative momentum flux, working against the source and driving the current leftward. As a measures the balance of these two fluxes, it controls how much fluid can turn left and how much must turn right. In the rigid-interface limit $a \rightarrow \infty$, vorticity is solely responsible for turning the current, and analytical solutions for steady boundary profiles are given by [Johnson and McDonald \(2006\)](#), with currents with Π positive turning right and those with Π negative turning left. The equations here are left in fully dimensional form and, noting that the evolution of an outflow depends only on a and the sign of Π , the dynamics are discussed over the full parameter range.

Long waves

Typically coastal outflows have a much larger along-shore extent than offshore. In this case, (4) can be replaced by

$$\frac{\partial^2 \eta}{\partial y^2} - \frac{1}{L_R^2} \eta = \begin{cases} \Pi, & 0 < y < Y, \\ 0, & y \geq Y, \end{cases} \quad (9)$$

and solved explicitly to give the streamfunction $\eta(x, y, t)$ for a current of width $Y(x, t)$

$$\eta = L_R^2 \Pi \left[\frac{e^{(y-Y)/L_R}}{2} + \left(\frac{Q}{L_R^2 \Pi} + 1 - \frac{e^{-Y/L_R}}{2} \right) e^{-y/L_R} - 1 \right]. \quad (10)$$

Using this expression in (7) and writing $Z(x, t) = \exp(-Y/L_R)$ gives the equation for the evolution of the current width

$$\frac{\partial Z}{\partial t} + \Pi L_R Z \left(1 + \frac{Q}{L_R^2 \Pi} - Z \right) \frac{\partial Z}{\partial x} = -\frac{Z^2}{L_R} \frac{\partial Q}{\partial x}. \quad (11)$$

Additionally, evaluating (10) at $y = Y(x, t)$ gives

$$Z^2 - 2 \left(\frac{Q}{L_R^2 \Pi} + 1 \right) Z + 1 = \frac{-2Q_e}{L_R^2 \Pi}, \quad (12)$$

giving $Z(x, t)$, and therefore the current width $Y(x, t)$, as a function of $Q(x)$ and $\eta(x, Y) = Q_e(x, t)$, the flux exterior to the current. For steady solutions, Q_e is a constant and (12) gives the steady current width.

JSM use (10)–(12) to construct the form of the variable-width steady solutions and the leading unsteady boundary profiles for arbitrary $Q(x)$, thus completely characterizing the ultimate evolution of the flow.

For simple source velocity profiles, they also find analytical expressions giving the full evolution of the outflow over time by following the characteristics of (11). Comparison of these long-wave results with contour dynamics simulations of the full problem show good agreement both in the evolution of the material boundary and in the velocity profiles. Here, a number of these results will be used, and the implications of (10)–(12) will be analyzed in an oceanographic context for outflows of variable strength or with alongshore currents.

The long-wave approximation is formally valid if the source width L is large compared to either the current width Y or the Rossby radius L_R . However, it also appears to be accurate for narrow sources. In fact, even with a point source ($L \rightarrow 0$), the interface Y is slowly and smoothly varying in the x direction, and JSM find that the long-wave approximation reproduces much of the evolution correctly. Thus, the precise details of the source velocity profile appear to have only a weak effect on the evolution of the outflow.

3. Constant strength sources without ambient currents, tides, or winds

This section describes the outflow behavior over the full range of a for the simple starting case of a constant flux source without the complicating effects of ambient currents, tides, or winds. If the expelled source fluid adjusts to a deeper-level, vortex stretching will generate positive relative vorticity. As the momentum flux is positive (section 3d) for positive perturbation PV, the current turns to the right. If the expelled fluid adjusts to a shallower level, vortex squashing will generate negative relative vorticity. For negative perturbation PV, the momentum flux can be negative and the current can turn to the left. The discussion here is thus split into three cases: zero PV outflow ($a = 0$), cooperative positive PV outflow, and competitive negative PV outflow. That is, after nondimensionalization, $\Pi = 0, \pm 1$.

a. Outflow of zero PV fluid

If the perturbation PV of the outflow fluid is zero, then it is simply passively advected by the source flow. The velocity field due to the source is derived in [appendix B](#). It gives an asymmetric outflow due to the rapid radiation of Kelvin waves. For a point source, a universal solution for this problem can be obtained by scaling lengths on L_R and time on L_R^2/Q_0 (a different scaling to that discussed earlier) and is shown in [Fig. 2](#). The outflow turns to the right and moves downstream in a thinning current with edge $x = x_e$, downstream given very closely by $x_e = (Q_0/L_R) \exp(-y/L_R)$. The flow cannot evolve to form a

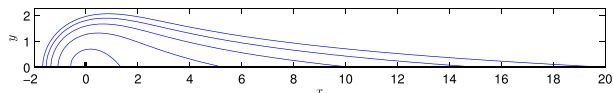


FIG. 2. Contour dynamics results showing the boundary of a zero PV outflow driven by a point source at the origin for non-dimensional times $t = 1, 5, 10, 15, 20$. In this and all subsequent figures, the coast is shown as a thick black line with a notch marking the position of the source.

steady, constant-width current and the bulge at the source grows indefinitely. The offshore extent of the bulge slows from fast initial growth to grow logarithmically in time, as can be seen by considering (B6) for $x = 0$ and noting that for $r \gg L_R$, $K_1(r/L_R)$ decreases exponentially in r . The boundary profile for small time is given by the rigid-interface solution: a growing semi-circle with radius $r = \sqrt{2Q_0t/\pi}$.

b. Outflow of positive PV fluid

If the outflow fluid has positive PV, then there is an additional flux of positive x momentum and the current is further driven rightwards under the influence of its image in the wall. The evolution of the expelled fluid for a range of a is shown in Fig. 3. For small a (large Kelvin number), vorticity is weak compared to the source and a solution similar to that for zero PV (Fig. 2) is found, except that, for nonzero a , a steady, constant-width current always forms. This steady current is led by a rarefying head with boundary profile accurately given by a similarity solution to (11) (see JSM). For large a (small Kelvin number), the flow is dominated by the vorticity that drives the flow rightward in a steady, constant-width current, led by a large eddy. The solution for $a = 5$ is close to that for the rigid-interface limit $a \rightarrow \infty$ discussed by Johnson and McDonald (2006).

The width of the steady current, which is the final state for all a and can be seen for $t = 30$ and $a = 1$ in Fig. 3, is given by setting $Q_e = 0$ in (12) to find

$$Y = L_R \cosh^{-1} \left(1 + \frac{Q_0}{\Pi L_R^2} \right). \quad (13)$$

The nondimensional steady current width $Y' = Y\sqrt{|\Pi|/Q_0}$ increases monotonically with the parameter a and tends to the limiting width of $\sqrt{2}$. In Fig. 4 this analytical solution is compared to the nondimensionalized average current widths from contour dynamics simulations. For all values of a the near-source bulge stops growing when it reaches the steady current width. At this point, the constant-width current is progressively established downstream, perturbed only by interfacial Rossby waves.

Figure 5a shows a satellite radar image of the surface-intensified outflow from the wide mouth of Chesapeake Bay. The region occupied by the expelled fluid downstream of the source bears a strong resemblance to QG positive PV outflow, shown in Figs. 5b and 5c for both a point source and for a finite width source with uniform outflow velocity profile, that is, $v(x, 0) = v_0$. Both the observations and simulations show a long, narrow outflow confined to the coast, slowly varying about a steady boundary profile and terminating in a rounded head. This rounded head is typical of the positive PV simulations presented here (see also Stern and Pratt 1985) and does not form for a zero PV outflow (cf. Fig. 2). Closer to the source, the comparison is not as good, with the Chesapeake plume displaying a localized bulge. Such a bulge has been shown to grow in size with increasing Rossby number, for example, experimentally by Horner-Devine et al. (2006) and in a 3D primitive equation numerical model by Fong and Geyer (2002). Such a finite Rossby number effect is not captured in our QG model.

A closer comparison of the observed and model velocity fields in the vicinity of the head of the current is shown in Figs. 6a and 6b, with arrows in Fig. 6a showing observed current speed and direction from later direct measurements, aligned to this satellite image. These show strong downstream flow near to the coast within the current, which weakens and turns away from the coast at the edge of the current. There is then a backflow of the ambient fluid around the head and back toward the source. This is typical of a current with positive vorticity, and although other factors such as wind may

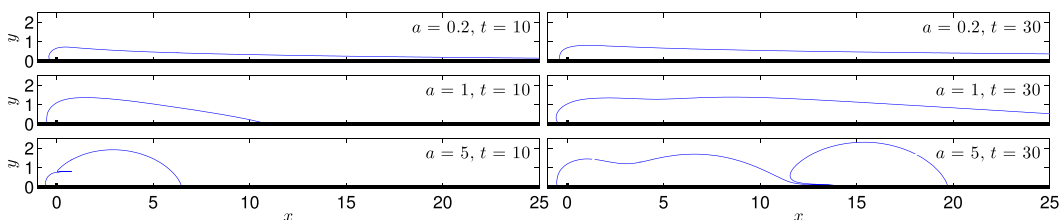


FIG. 3. The boundary of a positive PV outflow driven by a point source in contour dynamics simulations for $\Pi = +1$ and $a = 0.2, 1, 5$ at times $t = 10, 30$.

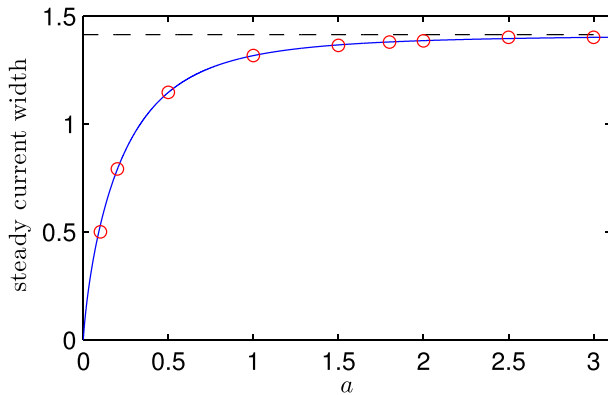


FIG. 4. The analytical solution for the nondimensional steady current width $Y' = Y\sqrt{|\Pi|/Q_0}$, where Y is given by (13), as a function of a (blue line) and the nondimensionalized average current widths in contour dynamics simulations (red circles). The limit $Y \rightarrow \sqrt{2}$ as $a \rightarrow \infty$ is shown as a black dashed line.

influence the surface velocity, these results match well with velocity vectors produced by the QG model and displayed in Fig. 6b.

c. Outflow of negative PV fluid

For outflows of fluid with negative PV, the vorticity contributes a flux of negative x momentum and drives the expelled fluid to the left, opposite to the rightward drainage pathway established by Kelvin wave radiation. The inverse Kelvin number a measures the relative importance of the vorticity-related momentum to the source-expelled momentum in the momentum balance. Thus, for small a (high Kelvin number) the fluid is expected to predominantly turn rightward and for large a (small Kelvin number) to turn left. The evolution of the expelled fluid boundary over time for various values of a is shown in Fig. 7. For small a , the source dominates and the outflow closely resembles the zero PV outflow in Fig. 2. For large a , the vorticity dominates and the flow is driven leftward, with the solution for $a = 5$ similar to the rigid-interface solution. For moderate values of a , a bi-directional current forms.

For $a \leq 1$, Fig. 7 shows the bulge near the source grows indefinitely with logarithmically growing offshore displacement. Thus, the source fluid is split between the growing bulge and the leftward and rightward currents. Steady, constant-width currents flowing both leftward and rightward are possible, but are not observed to form in the initial value problem for wide sources, as predicted by the long-wave theory. For narrow sources, contour dynamics results show that a steady leftward current can form but a steady rightward current has not been found for $a \leq 1$. The generic behavior for these currents is to form rarefactions, that is, thinning currents, the shape and velocity profile of which are accurately described by simple solutions of (11) (see JSM for details). Thus, for $a \leq 1$, the evolution is in general unsteady, the only exception being a section of steady leftward current in the case of a narrow source.

When $a > 1$, the interface near the source evolves to a steady boundary profile for all outflow velocity profiles. For wide sources this is given by the solution of (12) (see JSM), and for narrow sources it can be efficiently computed using the numerical scheme described in appendix D. These steady solutions are led, as seen in the $a = 0.2$ and $a = 1$ results at $t = 30$ in Fig. 7, by rarefying head profiles to each side, given by simple solutions of (11), again described in JSM. When a is above a critical value $a_c \approx 1.82$, the leftward rarefaction is overtaken and the steady solution terminates in a vortical head, as displayed for $a = 5$ in Fig. 7.

Outflows with negative PV closely resemble the numerical results of McCreary et al. (1997), who employ a 1.5-layer, variable density model to model freshwater outflows into a preexisting oceanic mixed layer of depth $H = 10$ m. They note that freshwater outflow is analogous to the source fluid having relatively low PV fluid, or fluid having negative vorticity anomaly in the terminology here. They find, in particular, upstream (leftward) turning of the outflow upon entering the ocean. A direct comparison with their results is made here using the same parameters used to produce Fig. 3 of their

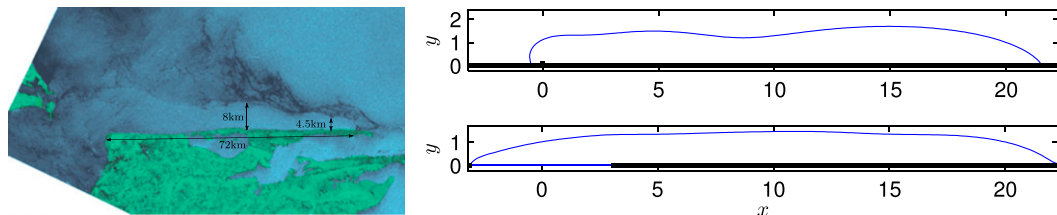


FIG. 5. Comparison of the Chesapeake Bay outflow to QG outflows. (a) A satellite radar image of the outflow from Chesapeake Bay turning rightward and forming a coastal current reproduced from Donato and Marmorino (2002). (b),(c) Contour dynamics simulations showing the boundary profiles of positive PV outflows from a (b) point source and (c) a uniform velocity source distributed from $x = -3$ to $x = 3$ at time $t = 30$ for $\Pi = +1$ and $a = 2$.

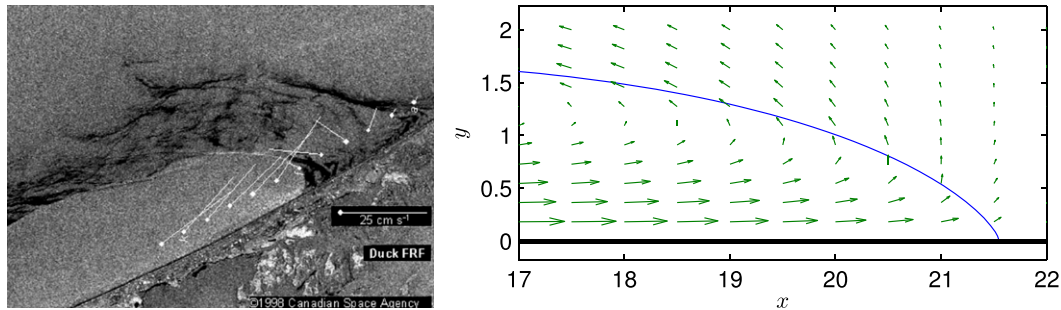


FIG. 6. Comparison of the head boundary profiles and velocities from (a) a satellite radar image of the head of the Chesapeake Bay outflow reproduced from Donato and Marmorino (2002) with white lines showing velocity vectors from later direct measurements and (b) the head from a contour dynamics simulation of a positive PV outflow from a point source for $\Pi = +1$ and $a = 2$ at time $t = 30$, with velocity arrows shown in green and the largest arrow indicating a nondimensional velocity of 0.9.

paper: an inflow volume flux of $10^{10} \text{ cm}^3 \text{ s}^{-1}$, which upon entering a mixed layer of depth 10 m, translates here to an area flux of $Q_0 = 10^3 \text{ m}^2 \text{ s}^{-1}$. In their experiment $\sqrt{g'H} = 80 \text{ cm s}^{-1}$ and $f = 8 \times 10^{-5} \text{ s}^{-1}$, implying a Rossby radius $L_R = \sqrt{g'H}/f = 10 \text{ km}$. Since McCreary et al. (1997) do not directly consider PV dynamics, the scale for relative vorticity $|\Pi|$ is less straightforward to estimate. A reasonable choice is $|\Pi| = 2 \times 10^{-5} \text{ s}^{-1}$, since it satisfies the QG requirement that $|\Pi|/f \ll 1$ and is compatible with relative vorticity generation by fluid column compression (as in Fig. 1c) by $\Delta H \approx 2 \text{ m}$ generating relative vorticity of order $f\Delta H/H \approx 2 \times 10^{-5} \text{ s}^{-1}$. With this choice, the dimensional length scale is $\sqrt{Q_0/|\Pi|} \approx 7.1 \text{ km}$, the inverse Kelvin number $a = L_R/\sqrt{Q_0/|\Pi|} \approx 1.4$, and the dimensional time scale $|\Pi|^{-1} \approx 0.58 \text{ days}$.

Figure 3 of McCreary et al. (1997), reproduced in Fig. 8a, shows a snapshot of the depth contours of the outflow at 40 days. To compare, the present model is run with source fluid having negative PV and $a = 1.4$ for 80 time units, or ≈ 46 days. The results are shown in Fig. 8b, where the plots have been inverted to enable direct comparison. The broad structures of the outflows are remarkably similar in displaying a wider, rightward upstream outflow with a thinner leftward-propagating plume driven by Kelvin wave propagation. After 40 days the outflow in Fig. 8b has spread upstream (positive x) a distance of 20 distance units, that is,

$\approx 140 \text{ km}$, which is less than the $\approx 240 \text{ km}$ upstream spread of the plume computed by McCreary et al. (1997). Some of this difference may be attributed to the choice of $|\Pi|$, and also to the fact that the McCreary et al. (1997) model is fully nonlinear, in contrast to the QG dynamics here. Indeed, some evidence for non-QG effects in the results of McCreary et al. (1997) are visible in the enhanced offshore spreading of the plume in McCreary et al. (1997), which, at 60 km after 40 days (Fig. 8a), is more than the $\approx 25 \text{ km}$ in Fig. 8b. McCreary et al. (1997) also run a “quasi linear” version of their model, in which momentum advection is neglected, with the same parameter values (see their Fig. 8) in which the maximum offshore spread of the outflow is $\approx 30 \text{ km}$, which gives further evidence for the offshore spreading of the outflow being a non-QG effect.

d. Momentum balance and the turning of outflows

Analyzing the momentum fluxes in a coastal outflow provides a useful tool to understand the turning of the current and the relative importance of different factors in controlling this. Appendix A considers a steady flow and integrates the nonlinear x -momentum equation of the rotating shallow water equations over the region S bounded by the curve ∂S , for either a large rectangular region or the region bounded by the outflow boundary $\partial \mathcal{S}$ and $x = \pm R$ for large R , and shows that QG flow trivially satisfies the leading-order geostrophic balance,

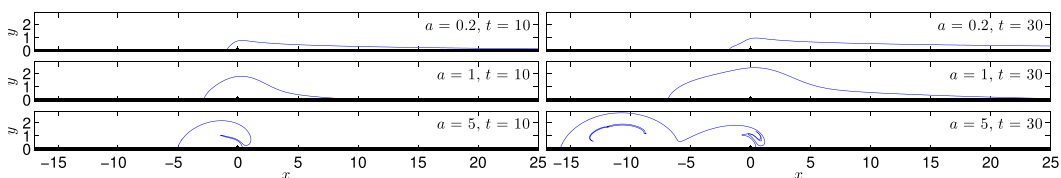


FIG. 7. Contour dynamics results showing the boundary of a negative PV outflow driven by a point source at the origin at times $t = 10, 30$, for $\Pi = -1$ and $a = 0.2, 1, 5$.

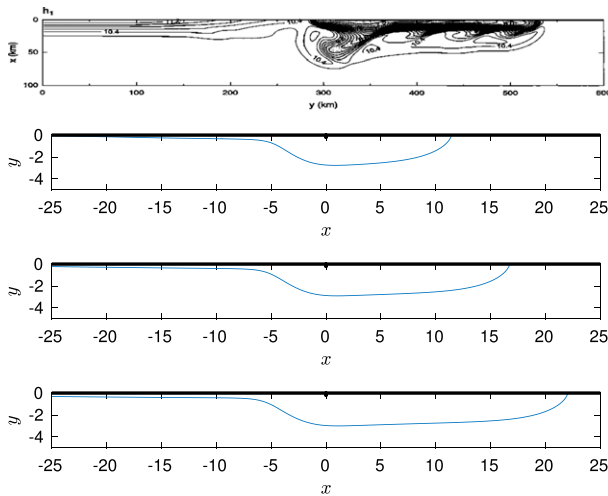


FIG. 8. (a) Reproduction of Fig. 3 of McCreary et al. (1997) showing depth contours of an outflow centered at $y = 300$ km. (b) Contour dynamics results showing the boundary of a negative PV outflow driven by a point source at the origin at times $t = 40, 60,$ and 80 (equivalent to 23, 35, and 46 days) for $\Pi = -1$ and $a = 1.4$.

but that a steady flow must also balance the momentum fluxes through the boundaries of the domain

$$\oint_{\partial S} uv \, dx = \oint_{\partial S} u^2 \, dy. \tag{14}$$

The first term in (14) is the x -momentum flux into the domain through the source, hereinafter labeled ΔM_s . The second term is the flux of momentum out of the domain in the downstream and upstream currents, hereinafter labeled ΔM_c . If the x -momentum flux through the source is positive then the current must ultimately turn rightward (where $dy > 0$); if it is negative then the current must turn left (where $dy < 0$). The current can be turned either by the effect of rotation or the vorticity of the current. For source velocity profiles where $v(x, 0)$ is symmetric in x , the source momentum will be zero and the current will be symmetric in x if $u(x, 0) = 0$ or $u(x, 0)$ is an odd function of x , as it is for outflows unaffected by rotation or vorticity. For flows affected by vorticity or rotation, $u(x, 0)$ has an even component that gives a momentum flux at the source and turns the current.

1) MOMENTUM FLUX DUE TO ROTATION

Appendix B derives the velocity field due to both finite width and point sources for QG flow. Equation (B8) gives the alongshore velocity u for a QG point source and shows that it consists of an odd singular component (second term), a finite odd component (third term), and a finite even component (first term). Close to the source the flow is dominated by the odd singular part,

but the finite even component still contributes to the momentum flux, and it is this ultimately responsible for turning the current. For finite width sources, (B5) shows that u has an even component equal to $Q_0 \exp(-y/L_R)/2L_R$ (as well as an odd component).

For a zero PV outflow, the velocity field is given by (B8) and (B6) so, far downstream, $\Delta M_c = Q_0^2/2L_R$ and, noting that the odd components of u contribute nothing to the integral, $\Delta M_s = Q_0^2/2L_R$, showing that momentum is conserved for this steady flow. For a finite-width symmetric source of zero PV fluid, the source flux is also equal to $Q_0^2/2L_R$ [the contribution from the first term in (B5); the second term is odd in x , so it makes no contribution] and the downstream flux is the same, so this steady solution also conserves momentum.

2) MOMENTUM FLUX DUE TO VORTICITY AND ROTATION

In section 3d(1), rotation was entirely responsible for turning the outflow. For vortical outflows, vorticity will also play a role in turning the outflow and for rigid-interface flows, rotation has no effect and vorticity is solely responsible for turning the flow. At the source, the integral of the product of the nonsymmetric u due to the vorticity and the singular v due to the source gives a momentum flux into the domain. For rigid-interface outflows, there is initially no momentum flux and the outflow is symmetrical. Over time the vorticity-driven cross-flow increases, increasing the momentum flux and turning the current rightward. The flow evolves to a steady state where the momentum fluxes at the source and downstream in the current match.

Johnson and McDonald (2006) give the analytical steady solution in complex variable form, written here for $\Pi > 0$:

$$z = \frac{i}{\pi} w_1 \log \left(\frac{w_1 - i\sqrt{2Q_0\Pi}}{w_1} \right) - \sqrt{\frac{2Q_0}{\Pi}} \frac{1}{\pi}, \tag{15}$$

which relates the position $z = x + iy$ to the function $w_1 = i\Pi y + v + iu$, which gives the velocity. As $z \rightarrow 0$, $w_1 \rightarrow \infty$, so expanding for large w_1 and small z gives

$$z = \frac{2iQ_0}{\pi w_1} - \frac{\sqrt{8Q_0^3\Pi}}{3\pi w_1^2} + O(w_1^{-3}), \tag{16}$$

which can be rearranged to give

$$w_1 = \frac{iQ_0}{\pi z} + \frac{i}{3} \sqrt{8Q_0\Pi} + O(z). \tag{17}$$

This form splits the velocity at the source into the irrotational, singular, symmetric component due to the

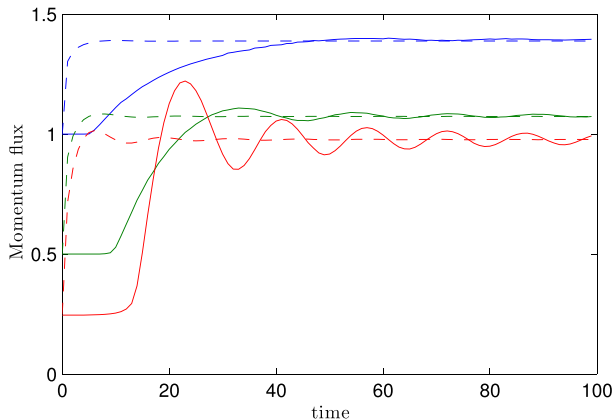


FIG. 9. Numerically computed horizontal momentum fluxes over time from the source ΔM_s (dashed) and across the line $x = 10$ ΔM_c (solid) for outflows with $Q_0 = 1$, $\Pi = 1$, and varying $a = 0.5$ (blue), 1 (green), and 2 (red).

source (first term) and the finite component due to the vorticity (second term), with u component equal to $\sqrt{8Q_0\Pi}/3$. Integrating this against the delta function offshore velocity gives the momentum flux $\Delta M_s = \sqrt{8Q_0^3\Pi}/3$. The downstream momentum flux can be computed by integrating the linear downstream velocity profile $u = \Pi(Y - y)$, where the downstream current width is $Y = \sqrt{2Q_0/\Pi}$, giving $\Delta M_c = \sqrt{8Q_0^3\Pi}/3$ and matching to the source momentum flux. Precisely the same results, but reflected in the y axis, are found for $\Pi < 0$.

For outflows of nonzero PV for finite a , both rotation and vorticity contribute to the source momentum flux and the turning of the current. The momentum fluxes for these outflows can be computed numerically. Examples of the evolution of the momentum fluxes over time are shown in Fig. 9 for $\Pi = +1$ and $a = 0.5, 1$, and 2. The momentum fluxes entering at the source and leaving downstream across the line $x = 10$ are plotted separately. When the currents reach a steady state, these two fluxes become equal with only some small oscillation in the downstream flux due to the interfacial Rossby waves. Initially, there is no momentum flux due to vorticity and the source and downstream fluxes are both equal to $Q_0^2/2L_R$, the zero PV fluxes. This initial value of ΔM_s as a fraction of the final value shows how important

rotation is in turning the current. The moment when the vortical current arrives at the line $x = 10$ can clearly be seen as a sharp increase in ΔM_c from $Q_0^2/2L_R$.

3) MOMENTUM BALANCE FOR LONG-WAVE SOLUTIONS

Appendix C calculates the momentum fluxes for steady long-wave solutions of (12) and (10) for a domain bounded by the outflow boundary $\partial\mathcal{D}$ and $x_1 < x < x_2$ for arbitrary x_1, x_2, L_R, Q_0 , and Π and an arbitrary source profile. The source flux is given by (C3) and the flux in the alongshore current is given by (C5), showing that, for all parameter values and source profiles

$$\Delta M_s(x_1, x_2) = \Delta M_c(x_2) - \Delta M_c(x_1), \quad (18)$$

and the flow conserves momentum.

The momentum imbalance paradox (Pichevin and Nof 1997) stems from assuming $u(x, 0) = 0$ and therefore neglecting the flux of momentum at the source. However, when this momentum flux is included, the paradox is resolved and steady solutions are in fact possible.

e. Steady boundary profiles

Appendix D presents a numerical scheme for computing the steady boundary of the outflow. Steady solutions for positive PV calculated using this method are shown and compared to contour dynamics results in Fig. 10. By time $t = 30$ the contour dynamics results are very close to the steady solutions with the only differences due to the initial transience, still visible in the form of interfacial Rossby waves moving to the right. The results of the iterative scheme for $a = 10^5$ were compared to the exact solution in the rigid-interface limit and found to be graphically indistinguishable.

Analytical solutions for steady boundary profiles in the rigid-interface limit $a \rightarrow \infty$ were derived by Johnson and McDonald (2006). For the limit $a \rightarrow 0$ and negative PV, a steady solution is not possible, and for positive PV and small a , rotation dominates over the vorticity and the asymptotic solution away from the wall is $\eta = \Pi L_R^2$ within the current, $\eta = 0$ outside, and by symmetry $\eta = \Pi L_R^2/2$ on the boundary, so the steady solution is given by the streamline of the flow due to the source with $\eta = \Pi L_R^2/2$.

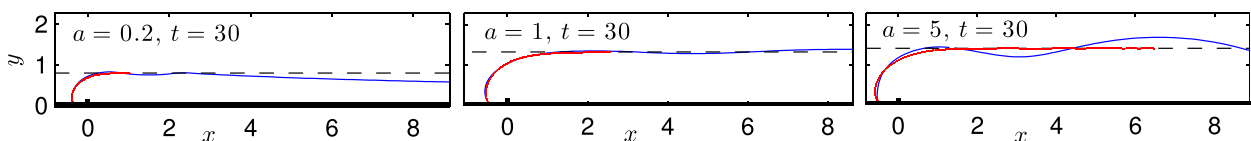


FIG. 10. A snapshot of the outflow boundary at $t = 30$ (solid blue line) computed with contour dynamics and the steady boundary profile (solid red line) computed with the iterative scheme for an outflow with $\Pi = +1$ and $a = 0.2, 1, 5$. The width of a steady x -independent current is shown as a dashed black line.

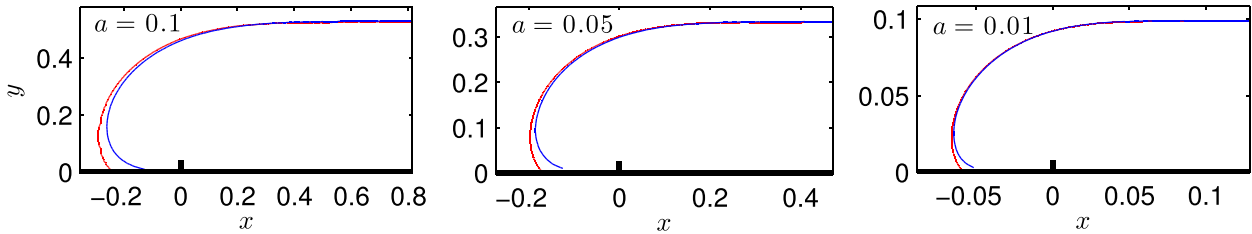


FIG. 11. The streamline with streamfunction value $\eta = 0.5IL_R^2$ (blue) and an iteratively computed steady boundary profile (red) for outflows with $\Pi = +1$ and (left to right) $a = 0.1, 0.05, 0.01$, showing the steady solution converging to the streamline of the source flow as a decreases.

Results showing the steady contour computed using this asymptotic solution for a point source, where the streamfunction due to the source is given by (B7), are compared to the iterative scheme in Fig. 11 for $a = 0.1, 0.05$, and 0.01 . Note that, for large x , this solution matches to the solution for a steady, constant-width current.

4. Unsteady sources, currents, winds, and tides

a. Variable-strength outflows

Changes in the volume flux of coastal outflows, which can vary by as much as an order of magnitude (Horner-Devine et al. 2015; van Maren and Hoekstra 2004), can be represented using a source with time-dependent strength. This section considers both strengths oscillating about an average value and those moving from one constant value to another as illustrative examples. A periodically varying outflow can be represented by a source with strength varying sinusoidally between two values Q_{\min} and Q_{\max} with period T , that is, a source with strength

$$Q_0(t) = \frac{Q_{\max} - Q_{\min}}{2} \sin\left(\frac{2\pi t}{T}\right) + \frac{Q_{\max} + Q_{\min}}{2}. \quad (19)$$

For zero PV outflows, the linearity of the problem means that, by the end of a period, a variable-strength outflow has evolved to the same boundary profile as a constant-strength source with the same average flux. It is only through interaction with the nonlinear vortical dynamics that varying the source strength can

change the evolution across a full period. Therefore, the source-dominated rightward rarefaction is expected to be relatively unaffected by the variable strength.

Figure 12 shows results for a strongly varying source ($Q_{\min}/Q_0 = 1/3, Q_{\max}/Q_0 = 5/3$) for a large range of periods ($T = 40, 10$, and 2) for an outflow of negative PV fluid. The boundary profiles are plotted at $t = 40$, where they have all completed an integer number of periods. While there is reasonable variability over an outflow cycle, by the end of a complete period the results are very similar, even for such a strongly varying source and such a large range of periods. The biggest differences from the constant strength source are the results for the longest period outflow $T = 40$, but even these are still very similar. This suggests that, at least for QG dynamics, oscillations of outflow strength may not be a significant dynamical factor and that models that average this outflow flux may be providing a good representation of the dynamics. Note that other studies of outflows with finite Rossby number (i.e., non-QG) have shown that the outflows can be substantially affected by low-frequency (subinertial) variability. For example, Yankovsky et al. (2001) show that the bulge, which is primarily an effect of finite Rossby number, may separate from the source region and be carried downstream.

The effects of varying outflow strength can be analyzed using long-wave theory. As an example, consider an outflow that starts at one strength Q_1 before smoothly changing to a second constant strength Q_2 , that is, the outflow with

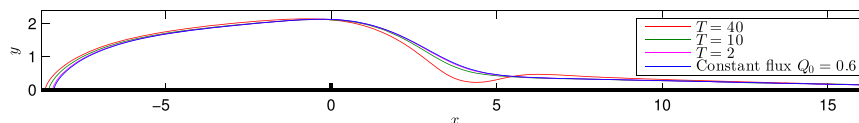


FIG. 12. A snapshot at $t = 40$ of the boundary of the expelled fluid of outflows with strength sinusoidally varying between $Q_{\min} = 0.2$ and $Q_{\max} = 1$ for variation periods $T = 40, 10, 2$ compared to a constant flux outflow of strength $Q_0 = 0.6$. In each case $\Pi = -1$ and $a = 1$.

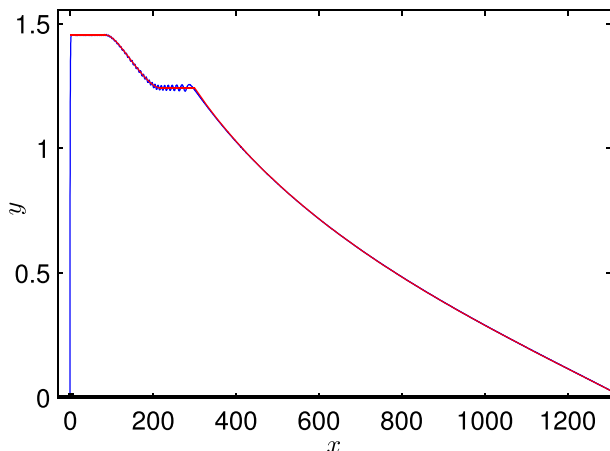


FIG. 13. A snapshot at $t = 750$ of an outflow for $a = 0.7$, $\Pi = +1$ with strength varying from $Q_1/Q_0 = 1$ for $t < 250$ smoothly up to $Q_2/Q_0 = 1.5$ for $t > 500$. The result of a contour dynamics simulation is shown in blue and the analytical solution is shown in red. Across the leading rarefaction and rear constant-width current these are indistinguishable. Note that the axes are scaled to fit the whole outflow.

$$Q_0(t) = \begin{cases} Q_1, & t \leq T \\ \frac{Q_1 + Q_2}{2} + \frac{Q_1 - Q_2}{2} \cos\left[\frac{\pi(t - T)}{T}\right], & T < t \leq 2T \\ Q_2, & t > 2T. \end{cases} \quad (20)$$

Provided that the time scale T is not small, the solution for this outflow is accurately given by the long-wave approximation and may be found analytically by integrating along the characteristics of (11) (see JSM for

the details of this procedure). An example comparing the analytical solution to contour dynamics for $a = 0.7$, $\Pi = +1$, $Q_1/Q_0 = 1$, $Q_2/Q_0 = 1.5$, and $T = 250$ is shown at time $t = 750$ in Fig. 13. The period $T = 250$ has been selected to best display the long time accuracy of the analytical solution.

The various boundary profile evolutions possible are best understood by analyzing the wave speed $c(Z) = \Pi L_R Z(1 + Q/L_R^2 \Pi - Z)$ of long waves from (11). This has a maximum at $Z = Q/2L_R^2 \Pi$, noting that $0 < Z \leq 1$, with $Z = 1$ corresponding to a zero width current and the current width increasing as Z decreases. This wave speed is displayed for the two cases $Q/L_R^2 \Pi \geq 1$ and $Q/L_R^2 \Pi < 1$ with positive PV in Fig. 14. The outflow in Fig. 13 corresponds to $Q/L_R^2 \Pi \geq 1$, where a thicker current close to the source (point A) is connected to a thinner current downstream (point B). As the wave speed increases in the downstream direction between the two, they can be joined by a rarefaction and the forward current can be joined by a rarefaction to the coastline (point C). If, however, the rear current was thinner (point B), it could not join smoothly to a thicker current downstream (point A) because the wave speed would decrease in the downstream direction and a shock would form. This shock would be resolved by the full two-dimensional dynamics into a series of waves. If $Q/L_R^2 \Pi < 1$, then the forward thinner current (point E) cannot connect to $Z = 0$; instead, it rarefies until near point F, where a shock forms. For $Q/L_R^2 \Pi < 1$, it is also possible to have smooth solutions with $Q_2 < Q_1$, where a thinner current near the source (point H) can smoothly join to a thicker current downstream (point G). This constant-width current cannot thin further, so it must

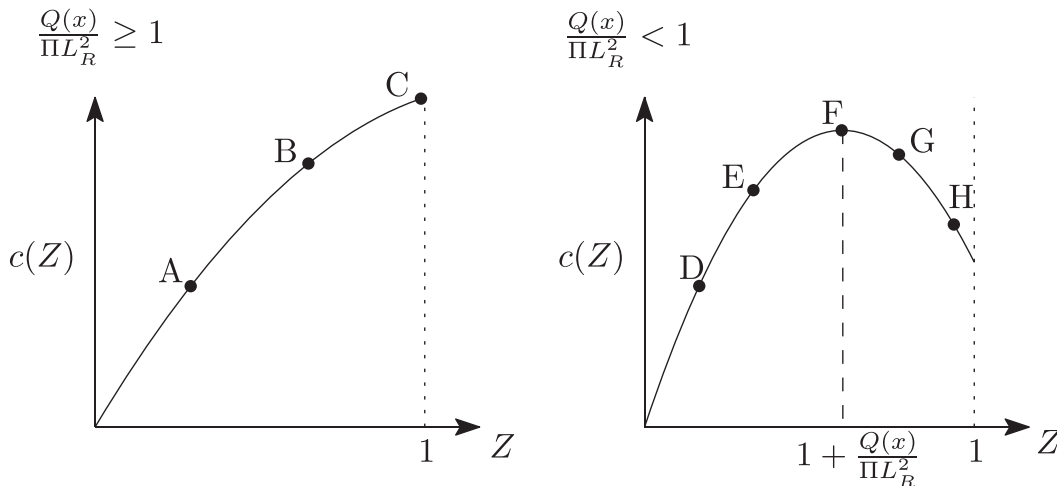


FIG. 14. The long-wave speed c as a function of $Z = \exp(-Y/L_R)$ for the two cases $Q(x)/\Pi L_R^2 \geq 1$ and $Q(x)/\Pi L_R^2 < 1$.

end in a shock. For negative PV, the wave speed can be negative, giving leftward currents with the analysis following similarly.

b. Alongshore currents

Ambient alongshore currents can have significant effects on coastal outflows. Downstream currents support the turning of the outflow and inhibit the growth of a bulge near the source. Fong and Geyer (2002) investigated the effects of a downstream current on a coastal outflow in a numerical model and found that even weak downstream currents were sufficient to halt bulge growth and confine all the outflow flux to the coastal current. Where the ambient current is oriented upstream, as in the case of the Columbia River outflow (Hickey et al. 2005), a bidirectional plume can be formed with a fraction of the outflow flowing upstream, a fraction downstream and, in some cases, a fraction feeding a growing bulge.

The effects of alongshore currents can be incorporated into the QG model by adding an additional background current with rightward flux Q_c . That is, a current with streamfunction

$$\eta_c = Q_c e^{-y/L_R}. \tag{21}$$

The results examined in section 3 are for the special case $Q_c = 0$. The case $Q_c = -Q_0$, an upstream current with flux equal to that of the source, is particularly interesting. Examining (B7) shows that this case is equivalent to the standard $Q_c = 0$ problem with the source velocity profile reflected in x (a Southern Hemisphere outflow). Thus, the outflow evolution for negative and positive PV are reversed for this value of Q_c . That is, the outflow evolution for $Q_c = -Q_0$, with generated vorticity Π , is identical to the outflow for $Q_c = 0$ with generated vorticity $-\Pi$, reflected in the y axis. Thus, the earlier results for negative PV can equally be interpreted as results for positive PV against an ambient current in the Southern Hemisphere.

For $Q_c = -Q_0/2$ the flow due to the source and current combined is symmetrical, so it contributes no momentum flux. Thus, as for rigid-interface outflows, the only asymmetry is due to the vorticity, and positive and negative PV outflows are simply reflections of each other. A zero PV ($a = 0$) outflow splits and flows equally left and right with an initially semicircular boundary profile that flattens over time into rarefying currents to the left and right.

For the rest of this section, just the case for positive PV is considered (negative PV solutions can be recovered by reflecting $Q_c \rightarrow -Q_0 - Q_c$ and $x \rightarrow -x$) and the outflow is a two-parameter problem dependent on

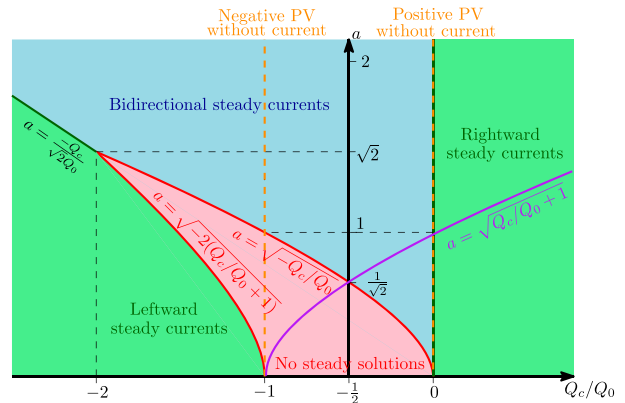


FIG. 15. A classification in $(Q_c/Q_0, a)$ space of the dynamical regimes displayed in an outflow with an ambient current of strength Q_c . Above the purple line rightward rarefactions must end in a shock.

a and Q_c/Q_0 . By analyzing the long-wave equations (12) and (11), the behavior of outflows can be classified in $(Q_c/Q_0, a)$ parameter space as shown in Fig. 15. The standard cases of a positive PV outflow without a background flow and a negative PV current without a background flow lie on the lines $Q_c/Q_0 = 0$ and $Q_c/Q_0 = -1$, respectively. Dependent on Q_c/Q_0 and a there is either a single rightward steady current (right-hand green region), steady currents in both directions (blue region), no steady currents (red region), or a steady leftward current (left-hand green region). The width and velocity profiles across these steady currents are the simple solutions to (12) and (10). These steady solutions join onto constant-width currents that are led by simple rarefying solutions to (11). The only exception is for $a \geq \sqrt{Q_c/Q_0 + 1}$ (the area above the purple line in Fig. 15), where the rightward steady current is led by a rarefaction that terminates in a shock. This corresponds to the situation in the second panel of Fig. 14, where a steady current (point E) rarefies to a shock (near point F) because the wave speed starts to decrease in the downstream direction. As a increases further the size of the rarefaction decreases until there is only a shock, which is resolved by the full two-dimensional dynamics to a head profile as seen in, for example, the lower panels of Fig. 3 and for rigid-interface outflows.

Thus, ambient currents can have very significant effects on the outflow dynamics when the flux they carry is comparable to the source flux. The outflow dynamics with an ambient current form four main behaviors, three of which (single rightward current, bidirectional currents, and no steady currents) have already been shown in detail in the earlier discussion of positive and negative PV outflows without ambient currents in section 3 (see Figs. 3, 7). An example of the final case, a leftward

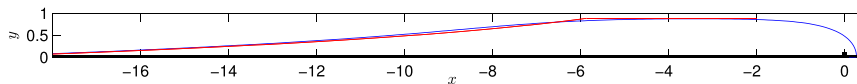


FIG. 16. A snapshot at time $t = 10$ of a contour dynamics simulation (blue) and the long-wave analytical solution (red) for an outflow from a point source for $\Pi = +1$, $a = 1$, with a background current of strength $Q_c = -2$. The equation $Q_c/Q_0 = -2$ is less than the critical value of $-3/2$, so a steady leftward current with constant width has formed, led by a rarefaction.

steady current, is shown in Fig. 16 for $\Pi = +1$, $a = 1$, and $Q_c/Q_0 = -2$. There is a steady boundary profile across the source region joining on its left to a steady, constant-width current led by a rarefaction that is accurately described by the analytical solution as shown.

The results here match well to those of Fong and Geyer (2002) and Hickey et al. (2005). Weak alongshore currents inhibit bulge growth and transfer the entire outflow flux into the downstream current in the simulations of Fong and Geyer (2002), corresponding to moving from the red area with a growing bulge in Fig. 15 to the green area $Q_c/Q_0 > 0$ when a small alongshore current is included. The introduction of an opposing current causes a bidirectional current to form both here and in the observations and simulations of Hickey et al. (2005).

c. Tides

Numerical models (Isobe 2005; Chen 2014) show that one of the main effects of tides on outflows is to increase the alongshore transport and reduce the growth of the bulge. This is supported by observations; for example, measurements of the strongly tidally influenced outflow of the Changjiang (Yangtze) River found 90% of the freshwater flux enters the coastal current (Wu et al. 2013). Isobe (2005) investigated the effect of tides and the role of inertial instability in the growth of the bulge in a numerical model for moderate Rossby number, finding that tides stabilized and halted the growth of the bulge and increased the alongshore transport. Isobe (2005, Fig. 14) shows model results for a variety of outflow and tidal strengths. The larger outflow results display the classic circular, inertia-driven bulge when the tidal forcing is weak. For stronger tidal forcing the bulge is broken up and the results start to resemble a lower Rossby radius outflow. For lower outflow velocity, Isobe's results, which have anticyclonic vorticity, look very similar to the QG outflows here with negative PV and low a (see, e.g., Fig. 7, $t = 10$, $a = 1$).

The effects of tides can be investigated using the present QG model by adding an additional periodically varying ambient current of the form

$$\eta_t = Q_t \sin(2\pi t/T) e^{-y/L_R}, \quad (22)$$

with maximum flux Q_t and period T . The term from (22) can be thought of as horizontally varying the position in

parameter space in Fig. 15, that is, periodically varying Q_c . This contrasts to variable strength outflow that was (see previous section) a vertical variation in $(Q_c/Q_0, a)$ parameter space, that is, varying a . Examples of solutions with this tidal forcing are shown in Fig. 17 for short and long periods $T = 1$ and 20 and various tidal strengths for a negative PV outflow.

There are many similarities to the variable strength outflows shown in section 4a. The longer the period of the forcing, the greater effect there is on the evolution of the outflow. Also, the right-hand rarefaction (which is dominated by the source) is again virtually unchanged by the forcing, which can only affect the ultimate outflow evolution through interaction with the nonlinear vortical dynamics. However, tides have a much more significant effect than a variable-strength outflow. Tidal forcing spreads the outflow horizontally, particularly in the direction of propagation due to the vorticity. This is achieved by inhibiting the growth of the bulge near the source. For long periods, a tide with maximum flux equal to that of the source is able to significantly disrupt the outflow. For short periods, the tide needs a flux order of magnitude larger than the source to provide significant disruption.

The average speed of a leftward vortical layer, as a function of the layer width Y , is proportional to $[1 - \exp(-Y/L_R)]^2/Y$, which has a maximum at $Y \approx 1.25643L_R$. If the current width, as the outflow is spread by tides, gets closer to this value then vorticity will drive the current further leftward, as seen in Fig. 17. However, if the unforced outflow is thinner than this value, then spreading the current will slow its leftward propagation and the tides will have less effect. An example of this situation for $a = 5$ is shown in Fig. 18. Here, a tide with

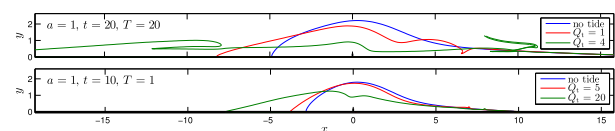


FIG. 17. Simulations of outflows for $\Pi = -1$ and $a = 1$, with tidal forcing of various strengths and periods. (top) A snapshot after one tidal period of an outflow with tidal forcing of period $T = 20$ and strengths $Q_t/Q_0 = 1$ and $Q_t/Q_0 = 4$ compared to the unforced case. (bottom) A snapshot at $t = 10$ of an outflow with tidal forcing of period $T = 1$ and strengths $Q_t/Q_0 = 5$ and $Q_t/Q_0 = 20$ compared to the unforced case.

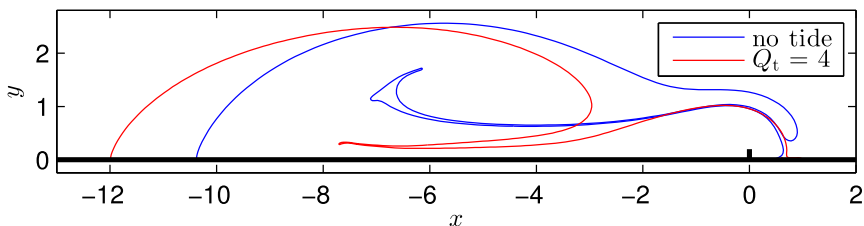


FIG. 18. A snapshot at $t = 20$ of simulations of a negative PV outflow for $\Pi = -1$ and $a = 5$ with (red) and without (blue) tidal forcing of strength $Q_t/Q_0 = 4$ and period $T = 20$.

strength $Q_t/Q_0 = 4$ and period $T = 20$ has much less effect than it did for $a = 1$ in the top panel of Fig. 17.

d. Wind forcing

Wind stress can significantly affect river plumes through the Ekman response of the near-surface fluid. Winds in the downstream direction push surface water toward the coast and drive downwelling, further focusing the outflow against the coast. Upstream winds have the opposite effect, pushing water and the coastal current away from the coast and driving upwelling. Typically, this results in currents separated from the coastline with rounded heads as seen in the observations of Gulf of Maine plume (Fong et al. 1997), Columbia River outflow (Hickey et al. 1998), and the Chesapeake Bay outflow (Dzwonkowski and Yan 2005), as well as in the numerical simulations of Hickey et al. (2005).

Dzwonkowski and Yan (2005) traced the outflow from Chesapeake Bay in satellite-measured ocean color data over time under varying wind conditions. Figure 19 reproduces their Fig. 8, which shows the plume evolution over 5 days. For the first 3 days there are southward winds driving downwelling or weak variable winds. For the fourth and fifth days, there are northward winds driving upwelling. Under downwelling-favorable winds, the current remains close to the coast and evolves similarly to the observations of Donato and Marmorino (2002) reproduced in Fig. 5 and the QG results presented above. Under the upwelling-favorable winds, surface water is pulled away from the coast and the plume quickly follows, moving away from the shore and retreating back toward the source. Its final boundary profile is much more rounded than the alongshore nose after day 3.

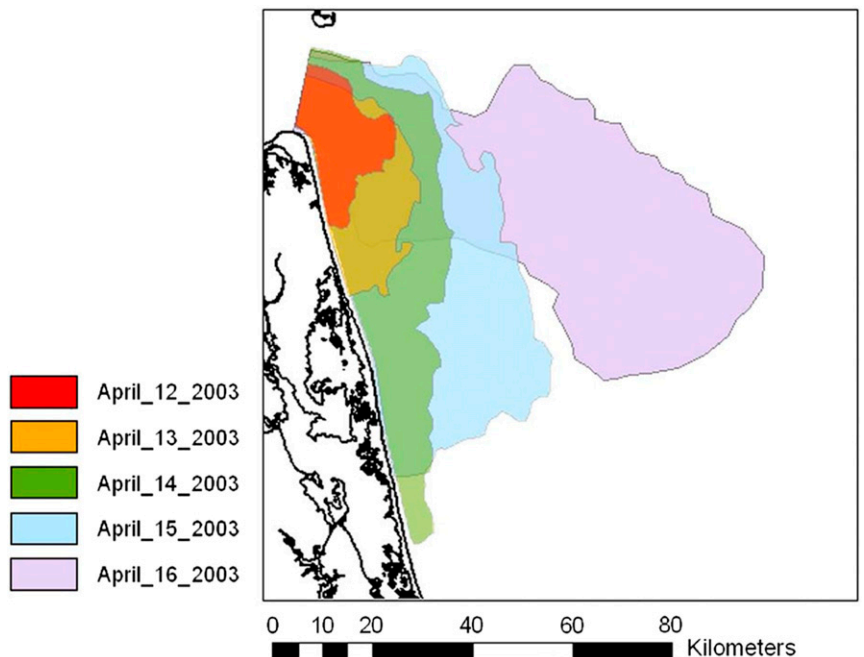


FIG. 19. Area of the Chesapeake outflow plume over 5 days with downwelling-favorable or varying winds becoming upwelling-favorable on the last 2 days, as measured by satellite-based ocean color data reproduced from Dzwonkowski and Yan (2005).

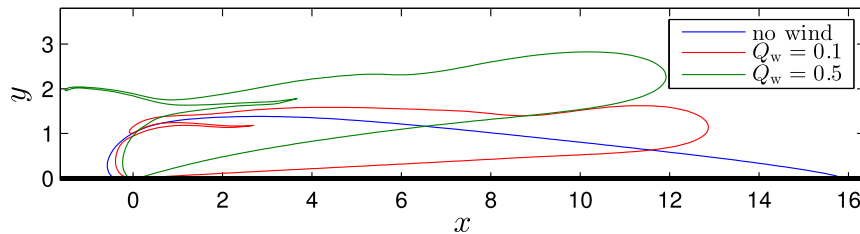


FIG. 20. Snapshots at time $t = 15$ of an outflow for $\Pi = +1$, $a = 1$, with wind forcing of strengths $Q_w/Q_0 = 0, 0.1$, and 0.5 .

The upwelling or downwelling caused by winds can be qualitatively represented in the present QG model by adding a continuous source along the extent of the coast. A source with flux per unit length Q_w/L_R through the wall $y = 0$ has streamfunction

$$\eta_w = \frac{Q_w}{L_R} x e^{-y/L_R}, \quad (23)$$

giving

$$\begin{pmatrix} u_w \\ v_w \end{pmatrix} = \begin{pmatrix} Q_w x/L_R^2 \\ Q_w/L_R \end{pmatrix} e^{-y/L_R}. \quad (24)$$

The streamfunction [(23)] is mathematically acceptable since it satisfies the governing QG equation [(4)], and the resulting offshore velocity [(24)] is realistic in displaying an exponential decay with offshore distance y . However, the alongshore component of velocity is linear in x , which is unrealistic, but for outflows that separate from the coast under upwelling (as happens here) this effect is relatively small since the alongshore velocity also decays exponentially in the y direction. Figure 20 shows an example of simulations with various wind strengths compared to the results without wind for an upwelling-favorable wind. The upwelling causes the expelled fluid to be pushed away from the coast and form an offshore current at an angle to the coast and with a rounded head similar to the observations shown in Fig. 19. As the wind strength increases, the current forms a larger angle to the coast and travels less distance alongshore.

5. Conclusions

This paper applies a simple QG model to investigate the dynamics of coastal outflows using contour dynamics simulations and the long-wave analytical solutions developed by JSM. This work has four main parts: first, the implications of the long-wave solutions are discussed in an oceanographic context. Second, the impacts of ambient currents, tides, winds, and variable

source flux are examined. Third, the momentum fluxes are considered, resolving the momentum imbalance paradox (Pichevin and Nof 1997) and showing that steady solutions are a robust feature of coastal outflows. Finally, a numerical scheme to compute steady solutions is developed. The simplicity of the model and the accuracy of the long-wave approximation mean that the dynamics can be fully understood and used to interpret observations, experiments, and more sophisticated and complex numerical models. Despite the simplicity of the model, it shows good agreement in comparisons with observations, experiments, and other numerical models.

The results are analyzed in detail for three primary problems: zero, positive, and negative PV, and a full range of the inverse Kelvin number $a = L_R \sqrt{\Pi/Q_0}$, which measures the relative importance of the vorticity to the source velocity. For zero PV, the outflow boundary profile grows offshore indefinitely with a long rarefying head to the right. For positive PV, both the source and the vorticity contribute positive x -momentum flux, and for all a , steady profiles eventuate with a constant-width coastal current led by either a rarefying head for low a or a rounded head for larger a . Downstream from the source, the outflow boundary profile and velocity fields match well to observations of the Chesapeake Bay outflow (Donato and Marmorino 2002). For negative PV, which can also be interpreted as a positive PV outflow working against an ambient current, richer dynamics are obtained due to the competing effects of the positive x -momentum flux from the source driving the flow rightward and the negative x -momentum flux from the vorticity driving it leftward, and bidirectional currents form. For $a \leq 1$ the near-source bulge grows indefinitely, with rarefactions carrying fractions of the flux leftward and rightward. For $a > 1$ the flow always evolves to a steady boundary profile across the source region, connecting to steady, constant-width currents both leftward and rightward, which are led by a rarefaction on the right and either a rarefaction (for smaller a) or rounded vortical head (for larger a) on the left.

With an understanding of the dynamics of these primary problems, other factors are then considered. The effects of an ambient alongshore current of strength Q_c are investigated, and the long-wave theory is extended to fully characterize the dynamics in $(Q_c/Q_0, a)$ space and four main dynamical regimes are identified: steady rightward currents, steady bidirectional currents, steady leftward currents, and unsteady growth. The outflows in each of these regimes are accurately described by analytical long-wave solutions that demonstrate the following interesting features: downstream ambient currents ($Q_c > 0$) suppress the growth of the bulge and encourage the growth of steady, constant-width currents containing the entire fluid flux, matching well to the results of [Fong and Geyer \(2002\)](#); upstream-flowing ambient currents lead to the formation of bidirectional steady currents as observed, for example, in the ambient-current-forced Columbia River outflow ([Hickey et al. 2005](#)). The results here support the conclusion of [Matano and Palma \(2010\)](#) that bidirectional currents are a feature of coastal outflows. These are observed in outflows from the Columbia ([Hickey et al. 2005](#)), Hudson ([Chant 2011](#)), and Changjiang (Yangtze) ([Beardsley et al. 1985](#)) Rivers.

Outflows with variable source flux are investigated for two illustrative problems: for a flux changing from one constant value to another, analytical long-wave solutions are found and demonstrated; and for a sinusoidally varying source flux, it is shown that, over a complete cycle, the outflow boundary does not vary significantly from a constant strength outflow with the same average flux.

A second important periodic forcing is that of tides. Here the effects of tides were represented as a sinusoidally varying alongshore current. These were found to have significant effects on the outflow boundary, halting the formation of the near-source bulge and spreading the fluid alongshore, matching well to the results of [Isobe \(2005\)](#). The effects of winds were also represented, showing that, for upwelling-favorable winds, the outflow fluid detaches from the coastline and forms a rounded boundary profile, matching well to observations from the Chesapeake Bay outflow ([Dzwonkowski and Yan 2005](#)) and observations and numerical simulations of the Columbia River outflow ([Hickey et al. 2005](#)).

Examining the momentum fluxes in the model highlights that rotation and vorticity both contribute to the shoreward turning of the current and shows that when the momentum flux at the source is included, steady solutions conserve momentum and the momentum imbalance paradox ([Pichevin and Nof 1997](#)) is resolved. This clarification enables progress toward understanding when either steady solutions or indefinitely

growing bulges form from outflows. The results here show that indefinitely growing bulges are not ubiquitous, but do form in a number of cases. An almost circular growing bulge forms when the outflow velocity is strong and inertia enters the dynamics at leading order. However, without inertia, it is still possible for bulges to grow indefinitely for outflows with zero PV or small negative PV ($a \leq 1$). The generation of vorticity is a stabilizing effect that halts the perpetual growth of bulges, leading to commonly observed steady, constant-width currents downstream of the source mouth.

Effects such as mixing, coastline shape, and bathymetry are not included here. Mixing can be highly complex and is driven by a number of factors. Some of those, such as winds and tides, are considered here but some, such as waves, bottom friction, and frontal processes, require more complex modeling. Coastline shape can strongly influence coastal currents. [Klinger \(1994\)](#) and [Sadoux et al. \(2000\)](#) investigated outflows of buoyant water that form geostrophic coastal currents before encountering a cape. At the cape, the flow was able to separate and form a growing gyre. These features may be common in coastal currents encountering capes or stepped coastlines ([Southwick et al. 2016](#)) and can be modeled using point vortex dynamics ([Southwick et al. 2015](#)).

The present model is aimed at surface-advected flows so the influence of bathymetry has not been included, although it is possible to represent some shapes of bottom topography in a QG model. [An and McDonald \(2004\)](#) and [An \(2004\)](#) consider outflows of vortical fluid into the coastal ocean with a shelf parallel to the coast with contour dynamics simulations and find that the shelf helps turn the current rightward. Thus, bathymetric steering may be a third mechanism affecting the turning of outflows.

Acknowledgments. We are grateful to the reviewers for their constructive comments. O.R.S. was supported by an EPSRC DTA studentship.

APPENDIX A

Integrated Momentum Balance for QG Flow

The nondimensional rotating shallow water equations for a layer with small perturbation η to a constant depth can be written

$$\varepsilon \frac{D\eta}{Dt} + (a^2 + \varepsilon\eta)\nabla \cdot \mathbf{u} = 0, \quad \text{and} \quad (\text{A1a})$$

$$\varepsilon \frac{D\mathbf{u}}{Dt} + \mathbf{k} \wedge \mathbf{u} = -\nabla\eta, \quad (\text{A1b})$$

where ε is the Rossby number and $a = L_R/\hat{L}$, for the length scale \hat{L} .

QG flow is obtained when $\varepsilon \ll 1$ by taking an asymptotic expansion of the form $\eta = \eta_0 + \varepsilon\eta_1 + \dots$, $\mathbf{u} = \mathbf{u}_0 + \varepsilon\mathbf{u}_1 + \dots$ giving, at leading order,

$$\mathbf{u}_0 = -\nabla \wedge (\eta_0 \mathbf{k}), \quad (\text{A2})$$

and at $O(\varepsilon)$

$$\frac{1}{a^2} \frac{D_0 \eta_0}{D_0 t} + \nabla \cdot \mathbf{u}_1 = 0, \quad \text{and} \quad (\text{A3a})$$

$$\frac{D_0 \mathbf{u}_0}{D_0 t} + \mathbf{k} \wedge \mathbf{u}_1 = -\nabla \eta_1, \quad (\text{A3b})$$

where $D_0/D_0 t = \partial/\partial t + (\mathbf{u}_0 \cdot \nabla)$. Thus, the leading order flow is geostrophic. The governing equation (conservation of PV) for η_0 [(2)] is found from (A3). Equation (A2) shows that QG flow satisfies the momentum equation [(A1b)] to leading order trivially. However, the next order balance in the momentum equation, given by (A3b), can also impose a condition on the leading-order flow.

Consider a steady outflow. Using the steadiness of the flow and the leading-order geostrophy, (A3a) implies that there exists a streamfunction ψ_1 for the $O(\varepsilon)$ flow, so $\mathbf{u}_1 = -\nabla \wedge (\psi_1 \mathbf{k})$. Integrating the x component of the momentum equation [(A3b)] over a control volume S with boundary ∂S for steady flow gives

$$0 = \iint_S u_0 \frac{\partial u_0}{\partial x} + v_0 \frac{\partial u_0}{\partial y} - v_1 + \frac{\partial \eta_1}{\partial x} dx, \quad (\text{A4})$$

$$= \iint_S \frac{\partial u_0^2}{\partial x} + \frac{\partial u_0 v_0}{\partial y} - \frac{\partial \psi_1}{\partial x} + \frac{\partial \eta_1}{\partial x} dx, \quad \text{and} \quad (\text{A5})$$

$$= -\oint_{\partial S} u_0 v_0 dx + \oint_{\partial S} u_0^2 - \psi_1 + \eta_1 dy, \quad (\text{A6})$$

where the continuity equation ($\nabla \cdot \mathbf{u}_0 = 0$) has been applied in the second line and Stokes' theorem has been applied in the third. The control volume can either be taken to be a large rectangle $-R < x < R$, $0 < y < H$ or the shape bounded by the outer boundary (a streamline) of the outflow, $-R < x < R$, $0 < y < Y$ for large R . Either way, the only boundaries contributing to the momentum fluxes are at the source and the upstream and downstream sections at $x = \pm R$ if ψ_1 is taken to be zero at the current edge. Where the current exits the domain, it has a constant width and is independent of x . Therefore, (A3b) implies that $\partial \psi_1(\pm R, y)/\partial y = \partial \eta_1(\pm R, y)/\partial y$, and it follows that $\psi_1(\pm R, y) = \eta_1(\pm R, y)$ as both η_1 and ψ_1 are 0 at the current edge. Note that η_1 and ψ_1 are not equal throughout the flow, only in the downstream sections (due to the x independence). Using this in (A6)

gives the integrated x -momentum equation for the leading order QG flow:

$$\int_{\partial S} u_0 v_0 dx = \int_{\partial S} u_0^2 dy, \quad (\text{A7})$$

which is unchanged when redimensionalized. Redimensionalizing, noting that the integrals along streamlines contribute nothing, and dropping the subscripts gives

$$\int_{-L}^L u(x, 0)v(x, 0) dx = \int_0^{Y(R)} u(R, y)^2 dy - \int_0^{Y(-R)} u(-R, y)^2 dy. \quad (\text{A8})$$

A steady QG flow that is x independent downstream of the source must satisfy this condition.

APPENDIX B

Flow Field due to the Source

a. General source velocity profile

The QG streamfunction η for the flow due to the source (with zero PV) satisfies the problem $\mathcal{L}\eta = (\nabla^2 - 1/L_R^2)\eta = 0$ with boundary conditions $\eta(x, 0) = Q(x)$ and $\nabla\eta \rightarrow 0$ as $y \rightarrow \infty$. Taking the Fourier transform (with transform variable k) in x of $\mathcal{L}\eta = 0$ gives

$$\hat{\eta}_{yy} - \left(k^2 + \frac{1}{L_R^2}\right)\hat{\eta} = 0. \quad (\text{B1})$$

which has the solution, satisfying the boundary conditions,

$$\hat{\eta}(k, y) = \hat{Q}(k)e^{-\kappa y}, \quad (\text{B2})$$

where $\kappa = \sqrt{k^2 + L_R^{-2}}$. Taking the inverse Fourier transform gives the streamfunction

$$\eta(x, y) = \frac{1}{2\pi} \int_{-\infty}^{\infty} \hat{Q}(k)e^{-\kappa y} e^{ikx} dk. \quad (\text{B3})$$

and using $\mathbf{u} = -\nabla \wedge (\eta \mathbf{k})$ gives the velocities

$$\begin{bmatrix} u(x, y) \\ v(x, y) \end{bmatrix} = \frac{1}{2\pi} \int_{-\infty}^{\infty} \begin{pmatrix} \kappa \\ ik \end{pmatrix} \hat{Q}(k)e^{-\kappa y} e^{ikx} dk, \quad (\text{B4})$$

for arbitrary $Q(x)$ [so long as $Q(x)$ decays to constant values as $|x| \rightarrow \infty$]. These integrals can be truncated and integrated numerically to give the velocity at any point.

For sources with outflow velocity $v(x, 0)$ symmetric in x , $Q(x) = Q_o(x) + Q_0/2$, where $Q_o(x)$ is an odd function and the velocities simplify to

$$\begin{bmatrix} u(x, y) \\ v(x, y) \end{bmatrix} = \frac{Q_0}{2L_R} \begin{pmatrix} e^{-y/L_R} \\ 0 \end{pmatrix} + \frac{i}{\pi} \int_0^\infty \hat{Q}_o(k) e^{-ky} \begin{pmatrix} \kappa \sin kx \\ k \cos kx \end{pmatrix} dk, \quad (B5)$$

showing that v is even in x and u is an odd in x function plus a function independent of x .

b. Point source

For a point source outflow, a neat form for the solution is obtained by exploiting linearity of \mathcal{L} and rewriting the problem for $v = \partial\eta/\partial x$ instead of η , giving $\mathcal{L}v = 0$ with boundary conditions $v = Q_0\delta(x)$ for $y = 0$ and $v \rightarrow 0$ as $y \rightarrow \infty$. Looking for a separable solution in terms of polar coordinates r and θ , satisfying the no-flux boundary condition and with the right singularity gives the solution

$$v = \frac{Q_0}{\pi L_R} K_1\left(\frac{r}{L_R}\right) \sin\theta, \quad (B6)$$

where K_n is the modified Bessel function of the second kind of order n . Integrating gives the streamfunction

$$\eta(x, y) = \frac{Q_0}{2} e^{-y/L_R} + \frac{Q_0 y}{\pi L_R} \int_0^x \frac{K_1(\sqrt{x'^2 + y^2}/L_R)}{\sqrt{x'^2 + y^2}} dx', \quad (B7)$$

splitting η into even (first term) and odd (second term) parts. Thus, $u(x, y) = -\partial\eta/\partial y$ is given by

$$u(x, y) = \frac{Q_0}{L_R} \left[\frac{e^{-y/L_R}}{2} + \frac{x K_1\left(\frac{r}{L_R}\right)}{\pi r} + \frac{1}{\pi L_R} \int_0^x K_0\left(\frac{\sqrt{x'^2 + y^2}}{L_R}\right) dx' \right]. \quad (B8)$$

APPENDIX C

Momentum Fluxes for Long-Wave Solutions

This appendix computes the momentum fluxes through the control domain $x_1 < x < x_2$, $0 < y < Y(x)$ for the steady analytical solutions in the long-wave limit for arbitrary L_R , Π , x_1 , x_2 , and source velocity profile $Q(x)$.

a. Source momentum flux

The horizontal momentum flux entering the domain from the source between two points x_1 and x_2 is given by

$$\begin{aligned} \Delta M_s &= \int_{x_1}^{x_2} u(x, 0)v(x, 0) dx \\ &= \int_{Q_1}^{Q_2} u[x(Q), 0] dQ, \end{aligned} \quad (C1)$$

since $v(x, 0) = \partial Q/\partial x$, where $Q_2 = Q(x_2)$ and $Q_1 = Q(x_1)$. The horizontal velocity at $y = 0$ as a function of Q , given by differentiating (10) and substituting Y from (12), is

$$u(Q) = L_R \Pi \sqrt{\left(1 + \frac{Q}{L_R^2 \Pi}\right)^2 - \left(1 + \frac{2Q_e}{L_R^2 \Pi}\right)}, \quad (C2)$$

where Q_e is the constant value of the streamfunction on the outflow edge $Y(x)$. Substituting (C2) into (C1) gives the momentum flux from source

$$\Delta M_s = \frac{L_R^3 \Pi^2}{2} [(s + 1)\mu + (2s_e + 1) \log(s + 1 - \mu)]_{Q_1/L_R^2 \Pi}^{Q_2/L_R^2 \Pi} \quad (C3)$$

using the substitution $s = Q/L_R^2 \Pi$ and $s_e = Q_e/L_R^2 \Pi$, $\mu = u(Q)/L_R \Pi = \sqrt{s^2 + 2(s - s_e)}$.

b. Alongshore momentum flux

The velocity $u(x, y)$ is found by differentiating (10) and substituting Z from (12). Integrating the square of this gives the horizontal momentum flux within the current

$$\begin{aligned} \Delta M_c &= \int_0^Y u^2 dy = (L_R \Pi)^2 \left\{ L_R Z \left(\frac{Q}{L_R^2 \Pi} + 1 - \frac{Z}{2} \right) \log Z \right. \\ &\quad \left. + \frac{L_R}{2} \left[\frac{1}{4} + \left(\frac{Q}{L_R^2 \Pi} + 1 - \frac{Z}{2} \right)^2 \right] (1 - Z^2) \right\}. \end{aligned} \quad (C4)$$

Using $Z = 1 + s - \mu$ and rearranging gives

$$\begin{aligned} \Delta M_c &= \frac{L_R^3 \Pi^2}{2} \left[(s + 1)\mu + \frac{1}{2}(s_e + 1) \right. \\ &\quad \left. + (2s_e + 1) \log(1 + s - \mu) \right]. \end{aligned} \quad (C5)$$

Note that this differs only by a constant, $(s_e + 1)/2$, from the indefinite integral in (C3), the expression for the source momentum flux, so the increment between the two stations x_1 and x_2 balances (18) and momentum is conserved for these steady flows.

APPENDIX D

An Iterative Scheme to Compute Steady Boundary Profiles

If a steady solution exists then its boundary $y \geq Y(x)$ is a streamline of the flow. The problem to solve for a steady boundary profile is

$$\mathcal{L}\eta = \begin{cases} 0, & y \geq Y(x) \\ \Pi, & 0 < y < Y(x), \end{cases} \quad (\text{D1})$$

where the operator $\mathcal{L} = \nabla^2 - L_R^{-2}$. This is combined with the boundary conditions that the streamfunction matches the far-downstream behavior of a constant-width current given by (10), $\eta = Q(x)$ on $y = 0$, $\eta \rightarrow 0$ as $y \rightarrow \infty$, and the additional condition that $\eta = Q_e$ on $y = Y(x)$. In a finite rectangular domain, these boundary conditions can be applied on the edges of the domain used to solve (D1).

A solution of this problem is found iteratively. Discretize the problem with first-order centered finite differences on a regularly spaced finite grid to give the matrix operator \mathbf{A} . Let $\boldsymbol{\eta}_n$ and $\boldsymbol{\Pi}_n$ be the vectors giving the value of the η and Π at each grid point at the n th iteration. Now for a given free surface, $\boldsymbol{\Pi}_n$ is known and the streamfunction can be found as $\boldsymbol{\eta}_n = \mathbf{A}^{-1}\boldsymbol{\Pi}_n$. The values of the streamfunction can then be used to update $\boldsymbol{\Pi}_n$ for the next iteration. Given $\boldsymbol{\eta}_n$, the location of the boundary Y can be identified, for each value of x , by tracking from large to small y and finding the first instance where $\eta > Q_e$. This point and all below it must be within the expelled fluid. Denote this approach as $\boldsymbol{\Pi}_{n+1} = \chi(\boldsymbol{\eta}_n)$. For positive PV, Y can be a multivalued function of x so the alternative method $\chi(\boldsymbol{\eta}_n) = \Pi H(\boldsymbol{\eta}_n)$, for the element-wise Heaviside function H [where the entries of $H(\mathbf{x})$ are 1 where the corresponding element of \mathbf{x} is strictly positive and 0 otherwise], is used. For improved stability, an underrelaxed version of the method can be used by updating $\boldsymbol{\Pi}_n$ at each time step with a fraction α based on this method (in the results below $\alpha = 0.05$ has been used) and a fraction $1 - \alpha$ of its previous value.

This method gives the iterative scheme

$$\boldsymbol{\eta}_n = \mathbf{A}^{-1}\boldsymbol{\Pi}_n, \quad (\text{D2a})$$

$$\boldsymbol{\Pi}_{n+1} = \alpha\chi(\boldsymbol{\eta}_n) + (1 - \alpha)\boldsymbol{\Pi}_n. \quad (\text{D2b})$$

For the initial value $\boldsymbol{\Pi}_1$ some approximation must be used. For positive PV the rigid-interface boundary profile, but scaled in size to match to the steady x -independent current, can be used, and for negative PV a smooth monotonic function matching the left and right steady solutions can be used. The entries of $\boldsymbol{\Pi}_1$ are Π if the grid point is within this contour and 0 if it is outside.

REFERENCES

- An, B., 2004: Modelling outflows, coastal currents and eddies. Ph.D. thesis, University College London, 169 pp. [Available online at <http://discovery.ucl.ac.uk/1446475/>.]
- , and N. R. McDonald, 2004: Coastal currents generated by outflow and vorticity and their interaction with topography. *Cont. Shelf Res.*, **24**, 1531–1547, doi:10.1016/j.csr.2004.05.002.
- Avicola, G., and P. Huq, 2002: Scaling analysis for the interaction between a buoyant coastal current and the continental shelf: Experiments and observations. *J. Phys. Oceanogr.*, **32**, 3233–3248, doi:10.1175/1520-0485(2002)032<3233:SAFTIB>2.0.CO;2.
- , and —, 2003: The characteristics of the recirculating bulge region in coastal buoyant outflows. *J. Mar. Res.*, **61**, 435–463, doi:10.1357/002224003322384889.
- Beardsley, R., R. Limeburner, H. Yu, and G. Cannon, 1985: Discharge of the Changjiang (Yangtze River) into the East China Sea. *Cont. Shelf Res.*, **4**, 57–76, doi:10.1016/0278-4343(85)90022-6.
- Chant, R., 2011: Interactions between estuaries and coasts: River plumes—Their formation transport and dispersal. *Water and Fine Sediment Circulation*, R. J. Uncles and S. G. Monismith, Eds., Vol. 2, *Treatise on Estuarine and Coastal Science*, Elsevier, 213–235, doi:10.1016/B978-0-12-374711-2.00209-6.
- , and Coauthors, 2008: Dispersal of the Hudson River plume in the New York Bight: Synthesis of observational and numerical studies during LaTTE. *Oceanography*, **21** (4), 148–161, doi:10.5670/oceanog.2008.11.
- Chapman, D. C., and R. C. Beardsley, 1989: On the origin of shelf water in the Middle Atlantic Bight. *J. Phys. Oceanogr.*, **19**, 384–391, doi:10.1175/1520-0485(1989)019<0384:OTOOSW>2.0.CO;2.
- Chen, S.-N., 2014: Enhancement of alongshore freshwater transport in surface-advected river plumes by tides. *J. Phys. Oceanogr.*, **44**, 2951–2971, doi:10.1175/JPO-D-14-0008.1.
- Davies, P., P. Jacobs, and L. Mofor, 1993: A laboratory study of buoyant fresh-water boundary currents in tidal cross-flows. *Oceanol. Acta*, **16** (5–6), 489–503.
- Donato, T. F., and G. O. Marmorino, 2002: The surface morphology of a coastal gravity current. *Cont. Shelf Res.*, **22**, 141–146, doi:10.1016/S0278-4343(01)00066-8.
- Dritschel, D. G., 1988: Contour surgery: A topological reconnection scheme for extended integrations using contour dynamics. *J. Comput. Phys.*, **77**, 240–266, doi:10.1016/0021-9991(88)90165-9.
- Dzwonkowski, B., and X.-H. Yan, 2005: Tracking of a Chesapeake Bay estuarine outflow plume with satellite-based ocean color data. *Cont. Shelf Res.*, **25**, 1942–1958, doi:10.1016/j.csr.2005.06.011.
- Fong, D. A., and W. R. Geyer, 2001: Response of a river plume during an upwelling favorable wind event. *J. Geophys. Res.*, **106**, 1067, doi:10.1029/2000JC900134.
- , and —, 2002: The alongshore transport of freshwater in a surface-trapped river plume. *J. Phys. Oceanogr.*, **32**, 957–972, doi:10.1175/1520-0485(2002)032<0957:TATOFI>2.0.CO;2.
- , —, and R. Signell, 1997: The wind-forced response on a buoyant coastal current: Observations of the western Gulf of Maine plume. *J. Mar. Syst.*, **12**, 69–81, doi:10.1016/S0924-7963(96)00089-9.
- Garvine, R. W., 1995: A dynamical system for classifying buoyant coastal discharges. *Cont. Shelf Res.*, **15**, 1585–1596, doi:10.1016/0278-4343(94)00065-U.
- Hacker, J. N., and P. F. Linden, 2002: Gravity currents in rotating channels. Part 1. Steady-state theory. *J. Fluid Mech.*, **457**, 295–324, doi:10.1017/S0022112001007662.
- Hermann, A. J., P. B. Rhines, and E. R. Johnson, 1989: Nonlinear Rossby adjustment in a channel: Beyond Kelvin waves. *J. Fluid Mech.*, **205**, 469–502, doi:10.1017/S0022112089002119.

- Hickey, B. M., L. J. Pietrafesa, D. A. Jay, and W. C. Boicourt, 1998: The Columbia River Plume Study: Subtidal variability in the velocity and salinity fields. *J. Geophys. Res.*, **103**, 10 339–10 368, doi:10.1029/97JC03290.
- , S. Geier, N. Kachel, and A. MacFadyen, 2005: A bi-directional river plume: The Columbia in summer. *Cont. Shelf Res.*, **25**, 1631–1656, doi:10.1016/j.csr.2005.04.010.
- Horner-Devine, A. R., 2009: The bulge circulation in the Columbia River plume. *Cont. Shelf Res.*, **29**, 234–251, doi:10.1016/j.csr.2007.12.012.
- , D. A. Fong, S. G. Monismith, and T. Maxworthy, 2006: Laboratory experiments simulating a coastal river inflow. *J. Fluid Mech.*, **555**, 203, doi:10.1017/S0022112006008937.
- , —, and —, 2008: Evidence for the inherent unsteadiness of a river plume: Satellite observations of the Niagara River discharge. *Limnol. Oceanogr.*, **53**, 2731–2737, doi:10.4319/lo.2008.53.6.2731.
- , R. D. Hetland, and D. G. MacDonald, 2015: Mixing and transport in coastal river plumes. *Annu. Rev. Fluid Mech.*, **47**, 569–594, doi:10.1146/annurev-fluid-010313-141408.
- Isobe, A., 2005: Ballooning of river-plume bulge and its stabilization by tidal currents. *J. Phys. Oceanogr.*, **35**, 2337–2351, doi:10.1175/JPO2837.1.
- Johnson, E. R., and N. R. McDonald, 2006: Vortical source-sink flow against a wall: The initial value problem and exact steady states. *Phys. Fluids*, **18**, 076601, doi:10.1063/1.2221353.
- , O. R. Southwick, and N. R. McDonald, 2016: Rotating vortical outflows. *J. Fluid Mech.*, in press.
- Klinger, B. A., 1994: Baroclinic eddy generation at a sharp corner in a rotating system. *J. Geophys. Res.*, **99**, 12 515–12 531, doi:10.1029/93JC03585.
- Kubokawa, A., 1991: On the behaviour of outflows with low potential vorticity from a sea strait. *Tellus*, **43A**, 168–176, doi:10.1034/j.1600-0870.1991.t01-1-00007.x.
- Lake, I., K. Borenäs, and P. Lundberg, 2005: Potential-vorticity characteristics of the Faroe Bank Channel deep-water overflow. *J. Phys. Oceanogr.*, **35**, 921–932, doi:10.1175/JPO2721.1.
- Lane-Serff, G. F., and P. G. Baines, 2000: Eddy formation by overflows in stratified water. *J. Phys. Oceanogr.*, **30**, 327–337, doi:10.1175/1520-0485(2000)030<0327:EFBOIS>2.0.CO;2.
- Lentz, S., 2004: The response of buoyant coastal plumes to upwelling-favorable winds. *J. Phys. Oceanogr.*, **34**, 2458–2469, doi:10.1175/JPO2647.1.
- , and K. R. Helfrich, 2002: Buoyant gravity currents along a sloping bottom in a rotating fluid. *J. Fluid Mech.*, **464**, 251–278, doi:10.1017/S0022112002008868.
- Marques, G. M., L. Padman, S. R. Springer, S. L. Howard, and T. M. Özgökmen, 2014: Topographic vorticity waves forced by Antarctic dense shelf water outflows. *Geophys. Res. Lett.*, **41**, 1247–1254, doi:10.1002/2013GL059153.
- Martin, J. R., and G. F. Lane-Serff, 2005: Rotating gravity currents. Part 1. Energy loss theory. *J. Fluid Mech.*, **522**, 35–62, doi:10.1017/S0022112004001351.
- , D. A. Smeed, and G. F. Lane-Serff, 2005: Rotating gravity currents. Part 2. Potential vorticity theory. *J. Fluid Mech.*, **522**, 63–89, doi:10.1017/S0022112004001363.
- Matano, R. P., and E. D. Palma, 2010: The spindown of bottom-trapped plumes. *J. Phys. Oceanogr.*, **40**, 1651–1658, doi:10.1175/2010JPO4352.1.
- McCreary, J. P., Jr., S. Zhang, and S. R. Shetye, 1997: Coastal circulations driven by river outflow in a variable-density 1/2-layer model. *J. Geophys. Res.*, **102**, 15 535–15 554, doi:10.1029/97JC00985.
- Nof, D., 1988: Eddy-wall interactions. *J. Mar. Res.*, **46**, 527–555, doi:10.1357/002224088785113540.
- , 2005: The momentum imbalance paradox revisited. *J. Phys. Oceanogr.*, **35**, 1928–1939, doi:10.1175/JPO2772.1.
- , and T. Pichevin, 2001: The ballooning of outflows. *J. Phys. Oceanogr.*, **31**, 3045–3058, doi:10.1175/1520-0485(2001)031<3045:TBOO>2.0.CO;2.
- , —, and J. Sprintall, 2002: “Teddiess” and the origin of the Leeuwin Current. *J. Phys. Oceanogr.*, **32**, 2571–2588, doi:10.1175/1520-0485-32.9.2571.
- Pichevin, T., and D. Nof, 1997: The momentum imbalance paradox. *Tellus*, **49A**, 298–319, doi:10.1034/j.1600-0870.1997.t01-1-00009.x.
- Rabalais, N. N., R. E. Turner, and W. J. Wiseman, 2002: Gulf of Mexico hypoxia, a.k.a. “the dead zone.” *Annu. Rev. Ecol. Syst.*, **33**, 235–263, doi:10.1146/annurev.ecolsys.33.010802.150513.
- Sadoux, S., J.-M. Baey, A. Fincham, and D. Renouard, 2000: Experimental study of the stability of an intermediate current and its interaction with a cape. *Dyn. Atmos. Oceans*, **31**, 165–192, doi:10.1016/S0377-0265(99)00032-9.
- Southwick, O. R., E. R. Johnson, and N. R. McDonald, 2015: A point vortex model for the formation of ocean eddies by flow separation. *Phys. Fluids*, **27**, 016604, doi:10.1063/1.4906112.
- , —, and —, 2016: A simple model for sheddies: Ocean eddies formed from shed vorticity. *J. Phys. Oceanogr.*, **46**, 2961–2979, doi:10.1175/JPO-D-15-0251.1.
- Spall, M. A., and J. F. Price, 1998: Mesoscale variability in Denmark Strait: The PV outflow hypothesis. *J. Phys. Oceanogr.*, **28**, 1598–1623, doi:10.1175/1520-0485(1998)028<1598:MVIDST>2.0.CO;2.
- Stern, M. E., and L. J. Pratt, 1985: Dynamics of vorticity fronts. *J. Fluid Mech.*, **161**, 513, doi:10.1017/S0022112085003032.
- Thomas, P. J., and P. F. Linden, 2007: Rotating gravity currents: Small-scale and large-scale laboratory experiments and a geostrophic model. *J. Fluid Mech.*, **578**, 35, doi:10.1017/S0022112007004739.
- Trenberth, K. E., L. Smith, T. Qian, A. Dai, and J. Fasullo, 2007: Estimates of the global water budget and its annual cycle using observational and model data. *J. Hydrometeorol.*, **8**, 758–769, doi:10.1175/JHM600.1.
- van Maren, D., and P. Hoekstra, 2004: Seasonal variation of hydrodynamics and sediment dynamics in a shallow subtropical estuary: The Ba Lat River, Vietnam. *Estuarine Coastal Shelf Sci.*, **60**, 529–540, doi:10.1016/j.ecss.2004.02.011.
- Whitehead, J., 1985: The deflection of a baroclinic jet by a wall in a rotating fluid. *J. Fluid Mech.*, **157**, 79–93, doi:10.1017/S0022112085002312.
- Wu, H., B. Deng, R. Yuan, J. Hu, J. Gu, F. Shen, J. Zhu, and J. Zhang, 2013: Detiding measurement on transport of the Changjiang-derived buoyant coastal current. *J. Phys. Oceanogr.*, **43**, 2388–2399, doi:10.1175/JPO-D-12-0158.1.
- Yankovsky, A. E., and D. C. Chapman, 1997: A simple theory for the fate of buoyant coastal discharges. *J. Phys. Oceanogr.*, **27**, 1386–1401, doi:10.1175/1520-0485(1997)027<1386:ASTFTF>2.0.CO;2.
- , B. M. Hickey, and A. K. Munchow, 2001: Impact of variable inflow on the dynamics of a coastal buoyant plume. *J. Geophys. Res.*, **106**, 19 809–19 824, doi:10.1029/2001JC000792.